

The Pennsylvania State University

The Graduate School

College of Engineering

**DEVELOPMENT OF AN ICE-PENETRATING SOFTWARE-DEFINED RADAR USING
THE UNIVERSAL SOFTWARE RADIO PERIPHERAL PLATFORM**

A Thesis in

Electrical Engineering

by

Peng Liu

© 2014 Peng Liu

Submitted in Partial Fulfillment
of the Requirements
for the Degree of

Master of Science

August 2014

The thesis of Peng Liu was reviewed and approved* by the following:

Sven G. Bilén

Associate Professor of Engineering Design, Electrical Engineering, and Aerospace Engineering
Thesis Adviser

Julio V. Urbina

Associate Professor of Electrical Engineering

Sridhar Anandkrishnan

Professor of Geosciences and Earth and Environmental Systems

Kultegin Aydin

Professor of Electrical Engineering

Head of the Department of Electrical Engineering

*Signatures are on file in the Graduate School.

ABSTRACT

An ice-penetrating software-defined radar has been developed using the Universal Software Radio Peripheral (USRP) that generates chirp signals. Called the USRP-based Ice Radar, the initial design goal was to create a portable, compact radar that is adaptable to future requirements using software-defined-radio techniques. The USRP-based Ice Radar will be used in polar glacier research to determine the depth of ice sheets up to 3 km. This version of the Ice Radar is built on previous versions that were hardware-based and PXI-based.

The systems functions by outputting a 20-W in-phase/quadrature chirp from a log-periodic antenna and receiving reflections with a second antenna of the same type. One channel has been established with a bandwidth of 5 MHz. The RF front-end paths have been designed to transmit and receive signals in the proper frequency range and includes a glacier/calibrate mode selection switch and blanking switch modules. An external FPGA has been implemented to generate the blanking switch signal, glacier/calibrate selection, 10-MHz reference clock, and a 500-Hz trigger signal. LabVIEW is used to generate the original chirp signal and to communicate with both the USRP and external FPGA.

Simulations were performed in LabVIEW to verify the function of the matched filter and SystemVUE was used to calculate gains in the transmission and receiving paths, and the losses due to the glacier and reflection from bedrock. Network and spectrum analyzers were used to verify the functions of transmitter and receiver paths in the frequency domain. The USRP-based Ice Radar is demonstrated to meet the design goals set out for it.

Table of Contents

List of Figures	v
List of Tables	vi
Acknowledgments	vii
Chapter 1 Introduction	1
1.1 Motivation	1
1.2 Achievements	2
1.3 Why USRP	3
1.4 Contributions of this Work	4
1.5 Thesis Overview	6
Chapter 2 Background	7
2.1 Theoretical Receiving Power	7
2.2 Permittivity and Conductivity Analysis	8
2.3 Electromagnetic Analysis	9
2.4 Loop Sensitivity	12
2.5 Range Resolution	13
2.6 Along-Track Resolution	17
2.7 Data from Antarctica	20
Chapter 3 System Design	22
3.1 USRP and Laptop	23
3.2 TX & RX Front-End Paths	26
3.2.1 TX Front-End Path	27
3.2.2 RX Front-End Path	28
3.3 Blanking Switch	32
3.4 Chirp Signal and Antennas	34
3.5 Maximum Direct Input Power	36
3.5.1 Direct Arrival Power	37
3.5.2 Air-Snow Reflection Arrival Power	37
3.6 SystemVUE Simulations	38
3.6.1 Simulation of Glacier Mode	38
3.6.2 Simulation of Calibrate Mode	40
3.7 Programming	42
3.7.1 LabVIEW Front Panel	44
3.7.2 Waveform Generation	47
3.7.3 TX/RX and External FPGA Synchronization	48
3.7.4 Data Acquisition Loop	52
3.7.5 Matched Filter	54
Chapter 4 System Test	57
4.1 USRP Output Power Test	57
4.2 USRP Direct Power Arrival	59
4.3 TX & RX Front-End Paths Tests	62
4.3.1 TX Front-End BPFs Performance Test	62
4.3.2 TX Network Analysis	63
4.3.3 RX Network Analysis	65
4.4 Blanking Switch and Glacier/Calibrate Mode Selection	66
4.5 Delay Line Test	70
Chapter 5 Discussion	72
Chapter 6 Conclusion and Future Work	74
Appendix: Bill of Materials	76
References	77

List of Figures

Figure 1-1 System Engineering V-Model	5
Figure 2-1 Matched Filtered Trace with Chirp Space of 450 ns	15
Figure 2-2 Matched Filtered Trace with Chirp Space of 500 ns	15
Figure 2-3 Matched Filtered Trace with Chirp Space of 550 ns	16
Figure 2-4 Matched Filtered Trace with Chirp Space of 450 ns	16
Figure 2-5 Matched Filtered Trace with Chirp Space of 500 ns	16
Figure 2-6 Matched Filtered Trace with Chirp Space of 550 ns	17
Figure 2-7 Along-Track Resolution vs. No. of Coherent Averages for Shallow Ice	18
Figure 2-8 Along-Track Resolution vs. No. of Coherent Averages for Middle Ice	18
Figure 2-9 Along-Track Resolution vs. No. of Coherent Averages for Deep Ice	19
Figure 2-10 Waveform of Captured Trace from PXI-based Ice Radar	20
Figure 2-11 Waveform of Matched Filtered Trace from PXI-based Ice Radar	21
Figure 3-1 Block Diagram of the Ice Radar System	22
Figure 3-2 NI USRP 2920 System Block Diagram	23
Figure 3-3 USRP 2920 Daughterboard WBX	24
Figure 3-4 USRP 2920 Motherboard with Xilinx Spartan 3A-DSP3400 FPGA	25
Figure 3-5 Power Spectrum of Signal Transmitted from USRP	27
Figure 3-6 TX Front-End Path Block Diagram	30
Figure 3-7 RX Front-End Path Block Diagram	31
Figure 3-8 Simulation of Matched-Filtered Trace for PXI-based Ice Radar	34
Figure 3-9 Simulation of Matched-Filtered Trace for USRP-based Ice Radar	35
Figure 3-10 I and Q values of I/Q Modulation	35
Figure 3-11 I/Q Modulator	36
Figure 3-12 Simulation of Channel Power along Glacier Mode Path	39
Figure 3-13 Simulation of Channel Power along Calibrate Mode Path	41
Figure 3-14 Flowchart of the Ice Radar System	43
Figure 3-15 LabVIEW Front Panel of Ice Radar System	46
Figure 3-16 USRP Setting Tab	47
Figure 3-17 Block Diagram of Chirp Pattern with Phase VI	49
Figure 3-18 Block Diagram of Waveform Generation	50
Figure 3-19 Block Diagram of TX/RX and External FPGA Synchronization	51
Figure 3-20 Chirp and Blanking Switch Control Synchronization	52
Figure 3-21 Block Diagram of Data Acquisition Loop	53
Figure 3-22 Block Diagram of Matched Filter Files	55
Figure 4-1 Spectrum Analyzer Display of USRP Outputs	58
Figure 4-2 USRP Direct Power Arrival Test without Offset	60
Figure 4-3 USRP Direct Power Arrival Test with Offset	61
Figure 4-4 USRP Direct Power Arrival Test with Delay	62
Figure 4-5 TX Front-End Band Pass Performance with Glacier Mode Output	63
Figure 4-6 TX Front-End Band Pass Performance with Calibrate Mode Output	63
Figure 4-7 TX Front-End Path Band Pass Performance	64
Figure 4-8 RX Front-End Path Band Pass Performance	66
Figure 4-9 Blanking Switch State in Glacier Mode	67
Figure 4-10 Blanking Switch State in Calibrate with 10 μ s Delay	68
Figure 4-11 Blanking Switch State in Calibrate with 1.5 μ s Delay	68
Figure 4-12 Blanking Switch State in Calibrate without Delay	69
Figure 5-1 TX & RX LEDs	73

List of Tables

Table 2-1 Permittivity, Conductivity, Electromagnetic Wave Parameter Values	11
Table 2-2 Parameters for Receiving Power Calculation	11
Table 2-3 Noise Figures and Gains of RX Path Components	13
Table 3-1 Ice Radar System Parameters	22
Table 3-2 USRP-External FPGA Communication Message Structure	33
Table 4-1 Chirp Amplitudes and TX Gains in Different Modes	59
Table 4-2 Delay Line Test Results	70
Table A-1 Bill of Materials	76

Acknowledgments

In completion of the USRP-based Ice Radar project and my master's degree, I have met many people who have given me valuable assistance. I would like to thank my parents, who have supported me at all times. I give my special thanks to my advisor, Dr. Sven Bilén, who generously helped me with my transition to Penn State, gave me the opportunity to work on this project, and provided all the help I needed. I would like to thank Dr. Sridhar Anandakrishnan, who gave thorough explanations such that I could understand the requirements, necessary functions, and working conditions of the Ice Radar system. I am grateful for help from Mr. Bob Capuro, who, with his extensive knowledge and experience, mentored me on technical issues and inspired me to find solutions to problems I encountered. I want to thank Mr. Jesus Mendoza, the designer of the PXI-based Ice Radar, who gave me real-time responses whenever I needed to understand the details of the PXI-based Ice Radar. I want to thank Mr. Hanxiong Hu, who assisted me in solving the blanking switch problem. Thanks to Mr. Peter Burkett who provided his experience with working in Antarctica and the materials needed in system tests and integration. I would like to thank Dr. Julio Urbina for providing my understanding of antennas. Thanks to all my friends and colleagues in the Systems Design Lab: Mr. Aaron Fleishman, Mr. Jesse McTernan, Mr. Mike Conway, and Mr. Khashayar Kotobi, who provided me with assistance from software to hardware, from system tests to thesis writing. Finally, thanks to all the friends who supported and encouraged me in overcoming every problem.

Chapter 1 Introduction

For the past several years, several versions of the Ice-Penetrating Software-Defined Radar (“Ice Radar”) have been designed and implemented in the Systems Design Laboratory (SDL) in Electrical Engineering department for Prof. Sridhar Anandakrishnan from the Penn State Ice and Climate Exploration (PSICE) program. The design goals have been focused on making the ice-penetrating radar to be compact, portable, flexible, and adaptable to future requirements. The first version of the Ice Radar used a National Instruments PXI chassis, along with PXI modules and controller for signal generation, signal receiving, processing, and storage. The PXI-based Ice Radar was finished in December 2012 [14], and was further modified during the summer of 2013.

To make the system smaller, easier to transport, lower cost, and more adaptable to future requirements, the second version described herein applied a Universal Software Radio Peripheral (USRP) as the signal transceiver. The current implementation combines the functions of the FlexRIO, digitizer, and arbitrary waveform generator PXI modules, performing waveform definition and post-processing on a laptop and chirp upconversion and downconversion on the USRP. The implementation of this USRP-based Ice Radar is described in this thesis.

1.1 Motivation

Ninety percent of the world’s freshwater is stored in the polar ice sheets, especially those of Antarctica and Greenland. The melting of the ice sheets results in rising sea levels, which will influence almost all aspects of human activity. Antarctic temperatures have been rising in the past century or so, resulting in an increase in the average sea level and a decrease in the extent of Arctic sea ice [1][2]. Hence, it has become urgent and of scientific value to carry out studies on polar ice sheets. However, because ice evolution occurs over such long periods—particularly for the shift from firn (a type of snow left over from past snowfalls) to ice, which takes from 190–200 years to 1000 years—scientific activities that cause damage to the ice sheet surface will interfere with the ice evolution process itself [3]. Thus, techniques and their related technology are needed that do not interfere with the evolution of ice.

Remote sensing is one method employed in ice sheet research that obeys the principle of causing no damage to ice evolution. Before radar sounding techniques were applied, methods such as seismic, gravitational, and magnetic methods were used. The characteristic of being able to make measurements continuously allowed this radar sounding equipment to be carried on moving vehicles and aircraft such that large swaths of ice could be examined. Thus, what has been termed radioglaciology has been widely applied.

1.2 Achievements

Since the 1960s, one of the research foci for glaciologists has been the internal structure of polar glaciers, such as density structure, bubbles, crystal orientation, and geochemical properties. Another focus is on stratification and temperature distribution. PSICE is a program that connects researchers from the departments of Geosciences, Geography, and Electrical Engineering at Penn State to work on the cryosphere. It houses some new interdisciplinary projects and acts as an interface to the Center for Remote Sensing of Ice Sheets (CReSIS). Current research includes ice sheet detection and modeling, determination of ice properties, glacial seismology, and measurements ice sheet flow. To perform ice sheet depth research, Prof. Anandakrishnan built a hardware-based ice-penetrating radar, which used an impulse transmitter and oscilloscope-based receiver [4].

A series of ice-penetrating radars, which were applied in the early stage of radar sounding research on Antarctic ice sheets, were introduced in [3]. Before the PXI-based Ice Radar was built, several ice-penetrating radars were designed and implemented by CReSIS, such as the series of synthetic aperture radars (SARs) for ice sheet basal measurements: the wideband SAR for depth sounding with chirp frequency of 120–300 MHz [17], the SAR for imaging polar ice sheets basal conditions [27], and the interferometric SAR for 3-D basal ice sheet imaging [34]. As software-defined radio (SDR) hardware has become more capable, especially with respect to the improvement in FPGA performance, the advantages and applicability of applying the SDR concept to ground penetrating radar has been discussed and solutions have been suggested [5], [6].

This concept was further enabled by the availability of the PXI integrated chassis and corresponding modules from National Instruments (NI). Based on the successful designs of the oscilloscope-based ice radar and from the CRISIS program, and combined with the advances of the SDR technique and PXI platform, the PXI-based Ice Radar was built. Measurements have been made in Antarctica during the winter of 2013. Reflected chirps were successfully captured, which inspired the development of the USRP-based Ice Radar, and provided abundant theoretical support to this project.

1.3 Why USRP

Although the PXI implementation can help achieve the goals of compact, flexible and portable, it still has several drawbacks from the perspectives of hardware and software. From the hardware perspective, it is still not small enough to be easily carried by researchers on flights into the field. Shipping the system can be done but requires significantly more time, which impacts logistics. In addition, although standard power cables and connectors are used, the existence of multiple connection pairs makes assembly complicated and time consuming. Moreover, the PXI-embedded controller is a duplication of resources considering that a laptop is still needed to remote login to it. From the software perspective, a significant number of changes to the software codes is needed when replacing the PXI with another SDR device, and for the FPGA programming, almost all codes need to be re-written.

Considering the drawbacks above, using the USRP has advantages in both hardware and software. For hardware advantages, it is about a tenth of the size of PXI chassis, which helps achieve the goals of compactness and portability. In addition, there are only four connections to the RF Front-end box and external blanking switch FPGA and one to the laptop. For software advantages, existing codes can be applied directly to any newer versions of the USRP, as the LabVIEW USRP toolkit is used and frequency parameters can be changed easily through the LabVIEW front panel. This is more advantageous than the PXI-based Ice Radar when it comes to the goal of adaptive to future requirements.

The USRP has been extensively applied as an affordable SDR device for education and research. LabVIEW and the USRP toolkits enable straightforward programming and code modification. The USRP has been used in applications such as GNSS signal generators [7] and receivers [8], cognitive radio [9], OFDM systems [10][11], weather surveillance [12], and ground-penetrating radar [13]. For ice-penetrating radar, however, it has not been extensively used. The limitation to the introduction of the USRP into the Ice Radar field lies in its low sampling frequency, which results in lower resolution. This USRP-based Ice Radar works at a 20-MS/s IQ rate, which results in temporal resolution of 0.05 μ s, or equivalently, a spatial resolution of 8.4 m. In this sense, this USRP-based Ice Radar is more of the stepping stone for future USRP device with higher IQ rate, such as can be provided by the NI USRP RIO. Only when changes of the field ice sheet depth are large enough within the designed detection range, and the accuracy of ice sheet depth is within the tolerance, can this radar be applied to gather data.

1.4 Contributions of this Work

This radar system includes eight major parts: 1) The high-performance laptop defines the parameters sent to the USRP and external blanking switch FPGA, and communicates with the USRP to transmit and receive traces. Post-processing of traces is carried out on the laptop. 2) The USRP up-converts, transmits, down-converts, and receives chirp signals according to parameters defined by the laptop. 3) The external blanking switch FPGA sends the receiver path blanking signal, calibrate/glacier mode selection signal, and a PPS and clock signal for synchronization and the phase-locked loop. 4) The RF Front-end Box includes the front-end TX and RX paths to block the carrier frequency and aliased frequency components from being transmitted from TX path; the blanking receiver path from receiving direct power from TX antenna; and amplifies weak chirp signals that are reflected from bedrock under the ice sheet. 5) The power amplifier receives a -7 -dBm chirp input and outputs a 20-W high-power chirp signal. 6) Antenna pairs transmit and receive chirp signals, and connect to the power amplifier and the RF Front-end box.

7) The power box is equipped with a standard interface and provides power at different voltages to the whole system. 8) The power amplifier switches are also built into this box to control whether or not the power amplifier is connected to the circuit. Apart from these eight parts, a U-blox GPS receiver is included to provide positioning information. LabVIEW is used for programming.

As with the PXI-based Ice Radar system, this system is built with commercial-off-the-shelf (COTS) components, allowing quick design, implementation, and modification. Three modes have been established, which allow for along-track resolution requirements of shallow (10 μ s), middle (25 μ s), and deep ice (50 μ s) depths. The number of coherent averages is defined using a long integer and is a trade off between along-track resolution and signal-to-noise ratio.

By following the system engineering V model [14][15], the Ice Radar system was designed, developed, integrated, and tested. Software such as SystemVUE was used in the design phase. Tests on single components and the entire system have been performed using hardware such as network and spectrum analyzers.

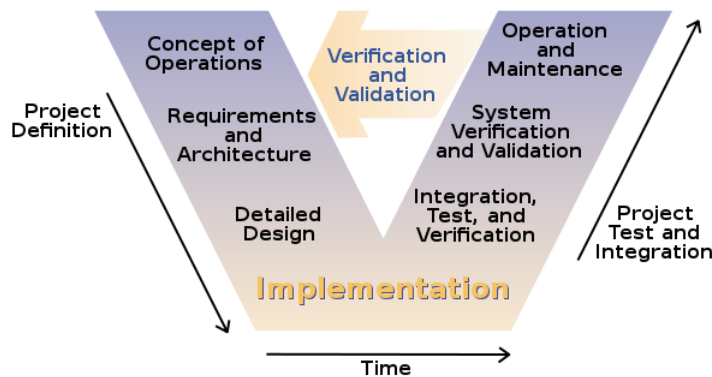


Figure 1-1 System Engineering V-Model

The Ice Radar system functions by calculating the averaged time difference between transmitted and received pulses to determine the depth of the ice sheet. Also, if stratification exists, multiple reflected chirps can be identified through a cross-correlation graph.

1.5 Thesis Overview

This thesis documents the development work of the Ice Radar, including technical background, theoretical analysis, system design, hardware selection, system test, and future adjustments. Chapter 1 introduces the design goals, design motivation, existing achievements, advantages and drawbacks of the USRP, and contributions of this project. Chapter 2 provides background and theoretical analyses for receiving power, permittivity and conductivity, electromagnetic wave propagation, loop sensitivity, range resolution, and along-track resolution. Chapter 3 includes information regarding system design, including introduction to the USRP, simulations of the TX and RX front-end loops, signal polarization and antennas, direct arrival signal power analysis, blanking switch, calibrate/glacier mode attenuation simulations, and all signal definition and post-processing codes. Chapter 4 explains all the system tests that have been carried out, including TX and RX path gain tests, blanking switch test, delay line test, and spectrum analyzer test. Chapter 5 discusses the performance of the system and Chapter 6 concludes this work and provides recommendations for future enhancements.

Chapter 2 Background

In order to demonstrate the feasibility of the USRP-based Ice Radar system and to provide support for the system design, this chapter presents relevant discussions on theoretical receiving power, permittivity and conductivity, electromagnetic wave propagation, loop sensitivity, range resolution, and along-track resolution. In addition, measurements made with the PXI-based Ice Radar are also introduced in this chapter, providing evidence of a successful design, and the feasibility of designing the USRP-based Ice Radar based on PXI-based Ice Radar.

The USRP-based Ice Radar system will generate a chirp with frequency range from 5 to 10 MHz, which is up-converted in the USRP to a carrier frequency of 142.5 MHz, making the output chirp frequency range of 147.5 to 152.5 MHz. Theoretical analyses are carried out based on this system specification.

2.1 Theoretical Receiving Power

Analysis of receiving power was developed for the PXI-based Ice Radar and are provided in [14]. Parameters are adjusted according to components that were replaced during system modification. Theoretical analysis of the receiving power is important in order to specify required transmitter (TX) power and in the design of the receiver (RX) front-end. If we assume a three-material ice sheet model, which contains air, solid ice, and bedrock, then the relationship between TX power (P_t) and RX power (P_r) can be expressed as Eqn. (2.1) [16]:

$$P_r = P_t \left(\frac{\lambda}{4\pi} \right)^2 \frac{G_t G_r T_{12}^2}{|2(h + Z / n_2)|^2 L_{ice}^2} |\langle R_{23} \rangle|^2, \quad (2.1)$$

where G_t (dBi) and G_r (dBi) are the gains of TX and RX antennas, respectively; T_{12} is the one-way power transmission coefficient from Medium 1 (air) to Medium 2 (ice); L_{ice} is the one-way dielectric loss in ice under a plane-wave approximation; $\langle R_{23} \rangle$ is the spatial average of the reflection coefficient from the bedrock; λ is the wavelength in ice; h is the height between the observation platform and the ice surface, which is the height of the phase center of the antenna to

the ice surface; Z is the distance from the system to the bedrock; and n_2 is the index of refraction at the air–ice surface.

The analysis below uses the assumption that the ice is at a temperature of -15 °C. The average antenna gain is 11 to 13 dBi. Here, 11 dBi is chosen as it is the more conservative value. The other values are: T_{12} is assumed to be 1.0 [14], n_2 is 1.78 for ice[3], h is 1.36 m, and Z is specified to be 3000 m. The one-way dielectric loss is [16]:

$$L_{\text{ice}} = e^{\frac{2\pi}{\lambda} Z \tan \delta}, \quad (2.2)$$

where $\tan \delta$ is the loss tangent of the ice. The expression $\tan \delta = \varepsilon'' / \varepsilon'$, with ε' and ε'' the real and imaginary parts of permittivity, respectively, with $\varepsilon' = \varepsilon_r' \varepsilon_0$ and $\varepsilon'' = \varepsilon_r'' \varepsilon_0$.

The spatial average of the reflection coefficient from the bedrock $\langle R_{23} \rangle$ is calculated as (from [17], which was first provided in [18]):

$$\left| \langle R_{23} \rangle \right|^2 = |R_{23}|^2 e^{-4\beta^2 \cos^2(\theta_i) S^2}, \quad (2.3)$$

where $|R_{23}|^2$ is the smooth interface power reflection coefficient. For frozen bedrock, $|R_{23}|^2$ is -28 dB [16]. β is the phase constant and θ_i is the incident angle, which is assumed to be 0° . S is the surface RMS deviation from the mean bedrock level, which is 0.1λ [17].

2.2 Permittivity and Conductivity Analysis

Dielectric absorption is one primary cause of signal attenuation, which is controlled by the dielectric constant, or permittivity, of ice [19]. The permittivity expression is:

$$\varepsilon = \varepsilon_r \varepsilon_0, \quad (2.4)$$

where ε_0 is the permittivity of free space, and ε_r is the relative permittivity. The complex relative permittivity expression is:

$$\varepsilon_r = \varepsilon_r' - j\varepsilon_r''. \quad (2.5)$$

Models for the real and imaginary values are given in [20]. The real part of the relative permittivity is linearly related to temperature via

$$\varepsilon_r' = 3.1884 + 0.00091T, \quad (2.6)$$

where T is in $^{\circ}\text{C}$. The imaginary part is split into two subparts, where the first represents the Debye-relaxation loss, while the second represents the infrared absorption loss, i.e.,

$$\varepsilon_r'' = \left(\frac{A}{f} \right) + Bf^C, \quad (2.7)$$

where f is in GHz, and A, B, C depend on temperature and purity of ice. The values of A, B and C at -15°C are 1.728×10^{-4} , $(4.696 \pm 0.500) \times 10^{-5}$, 1.056 ± 0.038 [21], respectively, in frequency range of 5 to 39 GHz, and the validity of these values at 150 MHz is discussed in [19] and [22].

The conductivity is related to the imaginary part of the permittivity is given by [22]

$$\sigma = 2\pi f \varepsilon_0 \varepsilon_r''. \quad (2.8)$$

Another model relating permittivity to temperature is given in [23], which connects one way power loss to temperature.

2.3 Electromagnetic Analysis

For a time-varying electromagnetic field, the wave functions in lossy, source-free media can be expressed as [24][25]:

$$\nabla^2 \vec{E} = \mu\sigma \frac{\partial \vec{E}}{\partial t} + \mu\varepsilon \frac{\partial^2 \vec{E}}{\partial t^2}, \quad \nabla^2 \vec{H} = \mu\sigma \frac{\partial \vec{H}}{\partial t} + \mu\varepsilon \frac{\partial^2 \vec{H}}{\partial t^2}, \quad (2.9a,b)$$

where μ is the permeability of the medium, which is assumed to be μ_0 for ice (μ_r for water is 0.999991 [24]). As the 5-MHz-bandwidth chirp is up-converted to a waveform with center frequency of 150 MHz, the electromagnetic field can be considered as a time-harmonic field with wave frequency of 150 MHz. The decoupled electric and magnetic fields of the wave equations can be expressed as:

$$\vec{E}(x,t) = \vec{E}_0 e^{j(kx - \omega t)}, \quad \vec{H}(x,t) = \vec{H}_0 e^{j(kx - \omega t)}, \quad (2.10a,b)$$

where k is the wavenumber and ω is the angular frequency.

In our case, as discussed in Section 2.2, a complex permittivity is involved; hence, the wavenumber is also complex. As discussed in [26], the complex wavenumber is given as

$$k^2 = \omega^2 \mu \varepsilon' \left(1 + \frac{\sigma}{j\omega \varepsilon'} \right). \quad (2.11)$$

The complex wavenumber can be written in the form of

$$k = k_+ + jk_-. \quad (2.12)$$

By substituting Eqn. (2.12) into Eqn. (2.10a,b), Eqn. (2.13a,b) are obtained:

$$\vec{E}(x,t) = \vec{E}_0 e^{-k_- x} e^{j(k_+ x - \omega t)}, \vec{H}(x,t) = \vec{H}_0 e^{-k_- x} e^{j(k_+ x - \omega t)}. \quad (2.13a,b)$$

The imaginary part of the wavenumber is responsible for attenuation, whereas the real part results in the phase constant. The wave properties can then be calculated using the real part, k_+ [25]:

$$v = \frac{\omega}{k_+}, \lambda = \frac{2\pi}{k_+}, n = \frac{ck_+}{\omega}, \quad (2.14a,b,c)$$

where v is the propagation speed in m/s, ω is the phase velocity in rad/s, λ is the wavelength in m, c is the speed of light, and n is the index of refraction.

After finding permittivity and conductivity, conductivity σ and complex relative permittivity ε_r can be obtained. These can then be applied in calculations of complex wavenumber and loss tangent, which are required for calculation of loss in the dielectric. From the electromagnetic analysis given above, we obtain also the wavelength, λ , which can be applied in Eqn. (2.2) to complete the calculation of dielectric loss. By applying λ and k_+ in Eqn. (2.3), we get the spatial average of the reflection coefficient. Table 2-1 provides values of permittivity, conductivity, and electromagnetic wave parameters.

Table 2-1 Permittivity, Conductivity, Electromagnetic Wave Parameter Values

Parameter	Value	Unit
ϵ_r'	3.17475	F/m
ϵ_r''	1.15833×10^{-3}	F/m
σ	9.65275×10^{-6}	S/m
k_+	5.59764	m^{-1}
k_-	-1.02117×10^{-3}	m^{-1}
λ	1.12247	m
$\tan \delta$	3.64857×10^{-4}	

We can now calculate the expected received power. The initial design specification is to provide 20 W output from the TX antenna. The power amplifier (PA) we are using in this USRP-based radar is the same one used in the PXI-based radar, which provides 50 dB gain at 150 MHz and maximum input of 0 dBm. The peak input power is set to -7 dBm, such that the peak output power is 43 dBm (20 W). The parameter values that are needed in Eqn. (2.1) are listed in Table 2-2. Using these values in Eqn. (2.1), the receiving power is calculated as -115 dBm

Table 2-2 Parameters for Receiving Power Calculation

Parameter	Value	Unit
P_t	43	dBm
λ	1.12247	m
G_t	11	dBi
G_r	11	dBi
T_{12}	1	
h	1.36	m
Z	3000	m
n_2	1.78	
L_{ice}	26.61	dB
$ \langle R_{23} \rangle ^2$	-34.86	dB

2.4 Loop Sensitivity

The calculation of loop sensitivity was carried out in order to make sure the USRP-based Ice Radar system not only will overcome spherical spreading, dielectric, and reflection losses, but also have sufficient signal-to-noise ratio (SNR) for data analysis. Loop sensitivity was set to 220 dB to meet the rough surface condition in Greenland [27], which is the same value applied in [17].

The loop sensitivity (LS) for the USRP-based Ice Radar system is calculated using:

$$LS = \frac{P_t G_t G_r N_{ave} G_{pc}}{P_{noise}}, \quad (2.15)$$

where N_{ave} is the number of coherent averages, G_{pc} is the power compression gain, and P_{noise} is the noise power of the receiver. Theoretically, the maximum allowable number of coherent averages is 2,147,483,647 ($2^{31} - 1$), considering the number is defined as a 32-bit signed integer. However, to be consistent with the PXI-based radar, we set it to be 65,536, which means N_{ave} in dB is 48.16 dB. Power compression gain $G_{pc} = \tau_{pulse} B$, where τ_{pulse} is the duration of pulse and B is the bandwidth of the chirp. The USRP-based Ice Radar system applies three chirp durations: 1 μ s, 3 μ s, and 5 μ s, and the up-converted chirp frequency is from 147.5 MHz to 152.5 MHz, so the bandwidth is 5 MHz. Thus, the maximum pulse compression gain is 25, or 13.98 dB. The pulse compression gain for a 3- μ s chirp is 60 (11.76 dB), which was used during the field test in Antarctica at the end of 2013.

The noise power of the receiver comes mainly from the receiver path in the RF front-end box. For each component, the noise factor can be calculated using

$$P_{noise} = kTBF, \quad (2.16)$$

where k is Boltzmann's constant (1.38×10^{-23} J/K) and $T = 258$ K. For a circuit path with cascaded devices, the Friis' formula for noise factor can be applied to calculate the total noise factor, i.e.,

$$F = F_1 + \frac{F_2 - 1}{G_1} + \frac{F_3 - 1}{G_1 G_2} + \dots + \frac{F_n - 1}{G_1 G_2 \dots G_{n-1}}. \quad (2.17)$$

In the receiver path a number of individual commercial-off-the-shelf (COTS) components are used. Their gains and noise factors are listed in Table 2-3. These values yield an overall noise factor of 3.95 or 6.0 dB, with total P_{noise} then calculated as -132 dBm.

Table 2-3 Noise Figures and Gains of RX Path Components

Components	NF (dB)	G (dB)
Switch	0	-1.1
BPF	0	-2.1
LNA	1.5	45
Switch	0	-1.1
Switch	0	-1.1
Amplifier	1.5	45
3-dB Attenuator	0	-3
Amplifier	1.4	12.5
BPF	0	-2.1
Limiter	0	-0.45

Using the values in Table 2-3 above, we obtain a loop sensitivity of 256 dB when the 3- μ s chirp is applied. To prove the sufficiency of this value in meeting the power losses and discernable SNR, data from [19] is referenced. The strength of basal echo from 3060 to 3090 m was from -200 to -170 dB, whereas the loss of the transfer function of the matched filtered strength data was from 166.8 to 174.6 dB in the frequency range from 110 to 500 MHz [19]. As the loop sensitivity value is >50 dB higher than these values, the USRP-baed Ice Radar system is shown to be able to detect signal echoes at a depth of 3000 m.

2.5 Range Resolution

Range resolution is the ability of a radar to distinguish two targets that are close to each other in range. The range resolution of a pulse compression radar is inversely proportional to the bandwidth of the pulse signal. This relation is expressed as [14]:

$$R = \frac{c}{2B}, \quad (2.18)$$

where B is the bandwidth of the pulse and c is the speed of light in the medium. To apply it in a pulse radar with duration of τ , the expression is:

$$R = \frac{c\tau}{2}. \quad (2.19)$$

When taking sampling rate into account, resolution degradation occurs, and we take this into account by writing [14]:

$$R = \kappa \frac{c}{2B}, \quad (2.20)$$

where $\kappa \geq 1$ represents the degradation of the signal due to sampling rate. As κ is introduced due to the limitation caused by sampling rate, the value is highly uncertain. Thus, simulations are necessary, with utilization of matched filter and repeated variation of pulse spacing and pulse amplitudes.

In the USRP-based Ice Radar system, a matched-filtering algorithm was implemented in LabVIEW and is used after the captured trace is transmitted to the laptop. When a trace is captured, cross correlation between the trace and the chirp is calculated, the peak of which indicates the time when the chirp return starts to be captured. The simulation is carried out as follows:

1. Two chirps with equal amplitudes are generated, each with frequency range from 5 MHz to 10 MHz, with sampling rate of 20 MHz.
2. Concatenate two zero arrays with same size to the front and end of the two chirps separately. The number of zeroes in the zero array represents the chirp space. Add these zero-padded chirps to create a trace with two partially overlapped chirps.
3. Attach two long zero arrays to the front and end of the trace created above. This creates a complete trace containing signals with and without chirps.
4. Using the matched filter that is programmed in LabVIEW to get the matched-filtered trace, keep increasing the chirp spacing until two peaks are discerned exactly at the times the chirps are supposed to be captured.

As 100 zeroes were padded to the head of the overlapped chirps, the first peak was supposed to appear at 5000 ns, considering the sampling rate was 20 MHz. The location of the second equal peak depends on the defined chirp spacing.

The simulation above was carried out for both the 3- μ s chirp and 5- μ s chirp modes. Results show that these chirp widths have little influence on the range resolution of the radar. The results are shown in Figures 2-1 to 2-6.

For the 3- μ s chirp mode, when the chirp spacing is increased from 450 ns to 500 ns, a clear peak shows up at 5000 ns and 5500 ns, as shown in Figure 2-2. By continuing to increase the chirp spacing, the first peak was clearly distinguished at 5000 ns and the second after the chirp spacing, as shown in Figure 2-3.

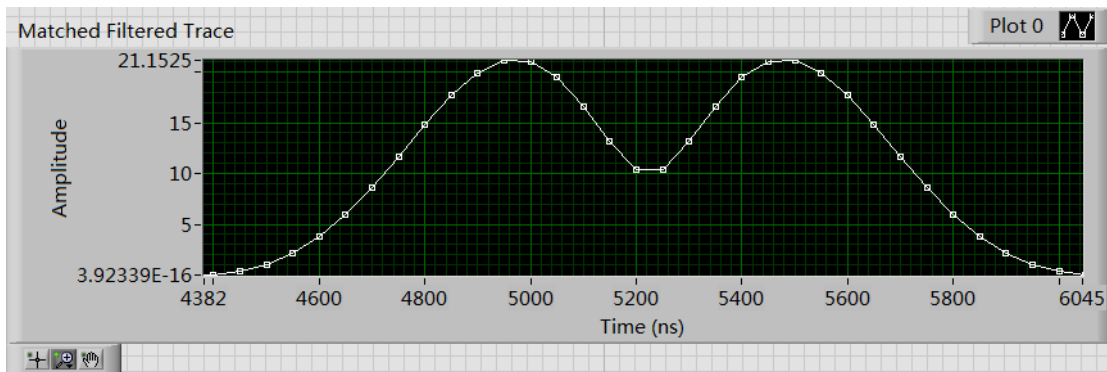


Figure 2-1 Matched Filtered Trace with Chirp Space of 450 ns

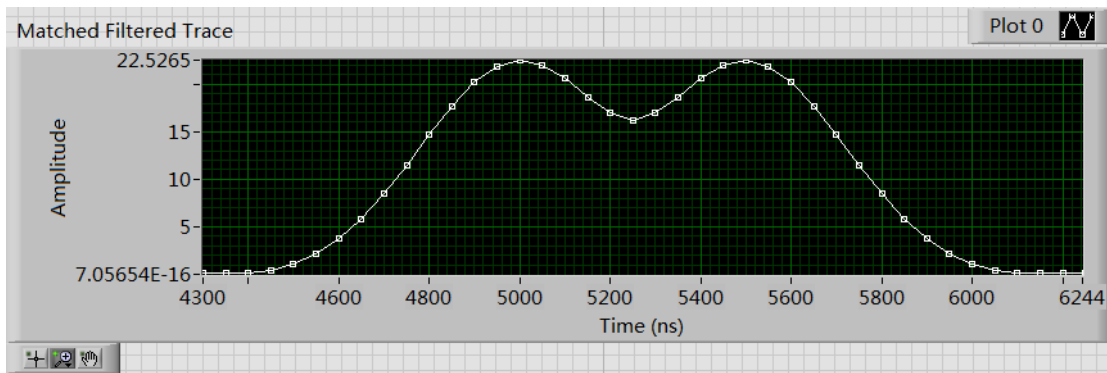


Figure 2-2 Matched Filtered Trace with Chirp Space of 500 ns

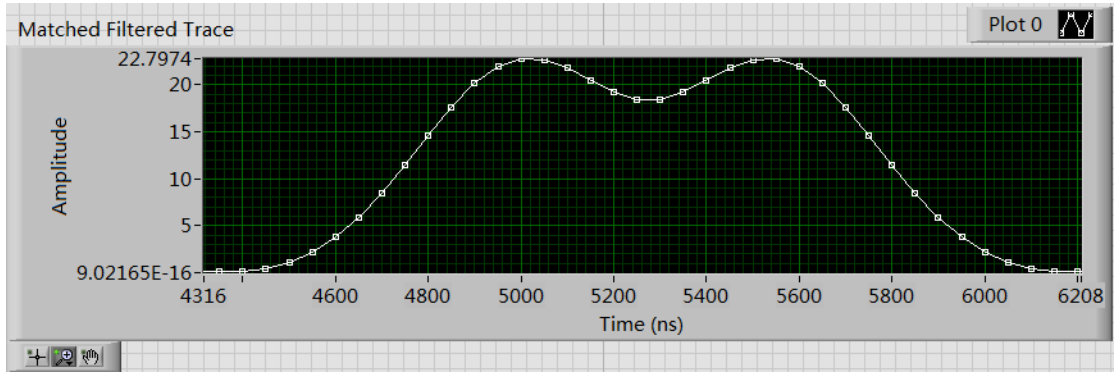


Figure 2-3 Matched Filtered Trace with Chirp Space of 550 ns

After repeating the solution by increasing the chirp width to 5 μ s, the same resolution was obtained.

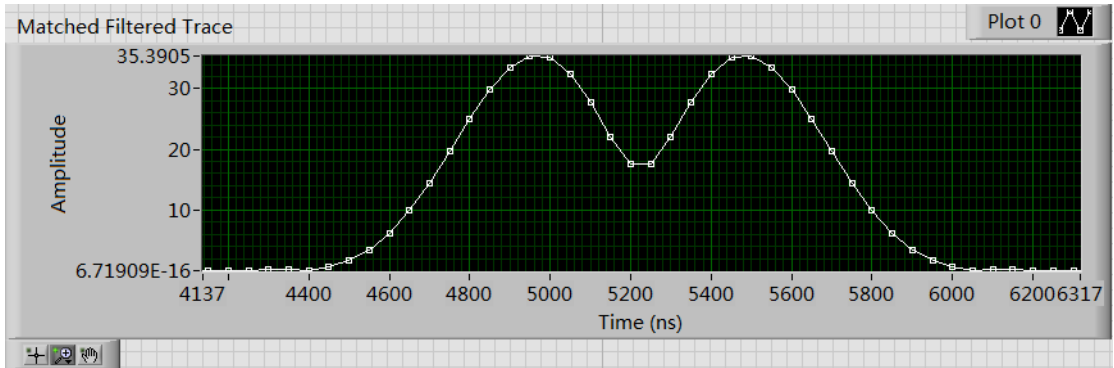


Figure 2-4 Matched Filtered Trace with Chirp Space of 450 ns

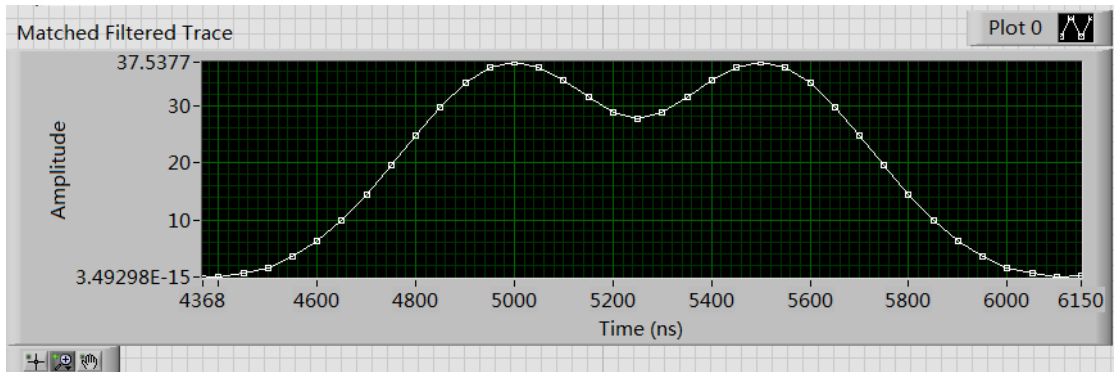


Figure 2-5 Matched Filtered Trace with Chirp Space of 500 ns

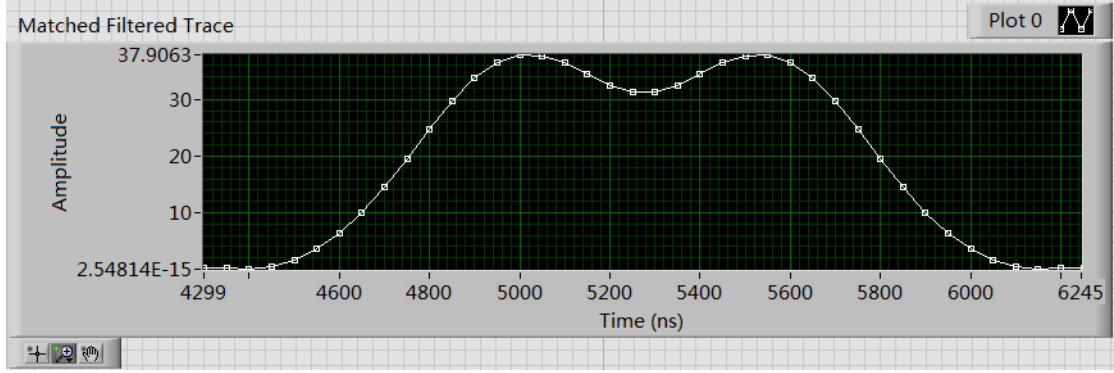


Figure 2-6 Matched Filtered Trace with Chirp Space of 550 ns

By comparing the cross correlations above, we can see that, for the same chirp spacing, the shape of the most significant curves are the same, with the only difference being amplitudes.

As 500-ns chirp spacing is selected by the above process, from which the range resolution can be readily calculated. The waveform propagation speed in ice is calculated from Eqn. (2.14a,b,c): $v = \omega/k_+ = 2\pi f_c/k_+ = 0.56c$, where c is the speed of light in free space. So the range resolution can be defined as $R = vt_{cs} = 0.56c \times 500 \text{ ns} = 28 \text{ m}$. Then Eqn. (2.20) can be adapted to the form that fits waveform transmission in ice to find $R = \kappa c/2B = \kappa 0.56c/(2 \times 5 \text{ MHz}) = 0.56c \times 500 \text{ ns}$, which means $\kappa = 5$.

2.6 Along-Track Resolution

As azimuth resolution represents the ability of a radar to distinguish two reflectors at similar ranges but different bearings from one reference point [28], the radar is usually regarded as a single static detector, and the calculation of the resolution is through the antenna azimuth beamwidth and the slant range of the second reflector.

For a moving radar, such as the Ice Radar on a travelling snowmobile, the term along-track resolution is applied [14]. It describes the distance covered during a single averaged trace, and beamwidth is not taken into consideration. As discussed in Section 2.5, N_{ave} coherent averages are carried out to improve the SNR. Considering the time duration t for each signal collection is $10 \mu\text{s}$, $25 \mu\text{s}$, or $50 \mu\text{s}$, the time for each average is $N_{\text{ave}} \times t$, and the along-track resolution is:

$$R_{\text{AT}} = v_{\text{radar}} N_{\text{ave}} \times t. \quad (2.21)$$

When the radar is moving at the speed of 10 km/h, the along-track resolution versus number of coherent averages for those three modes are shown in Figures 2-7 to 2-9.

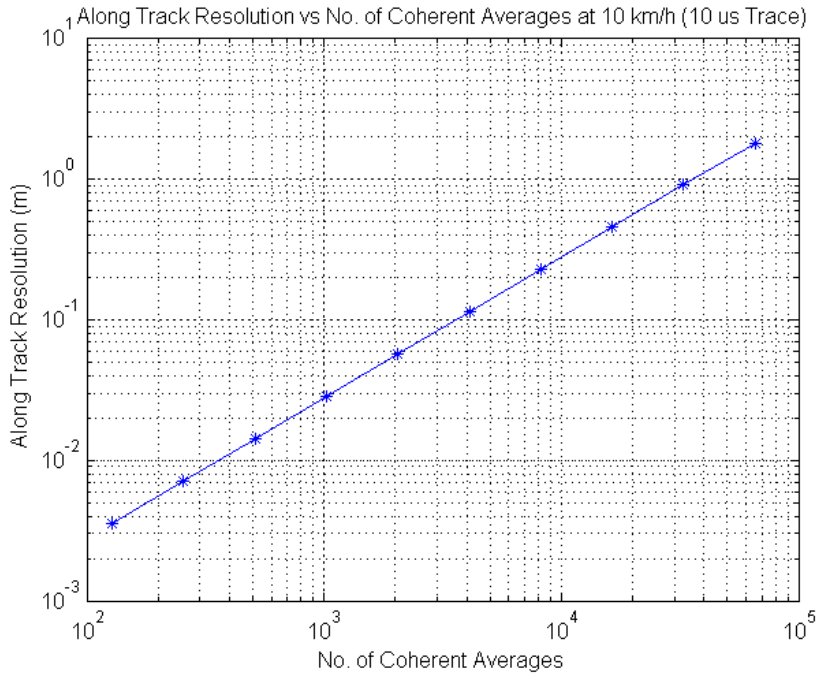


Figure 2-7 Along-Track Resolution vs. No. of Coherent Averages for Shallow Ice

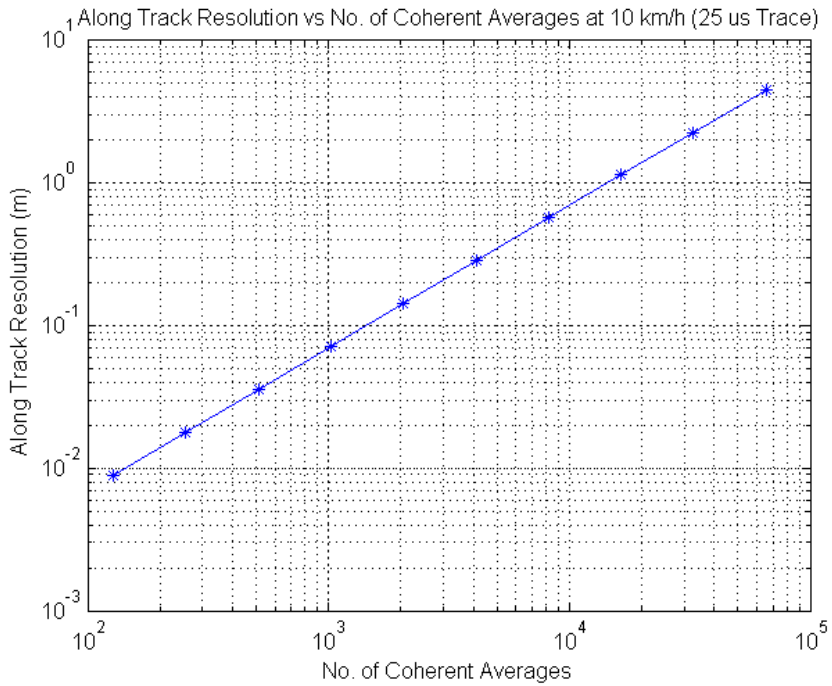


Figure 2-8 Along-Track Resolution vs. No. of Coherent Averages for Middle Ice

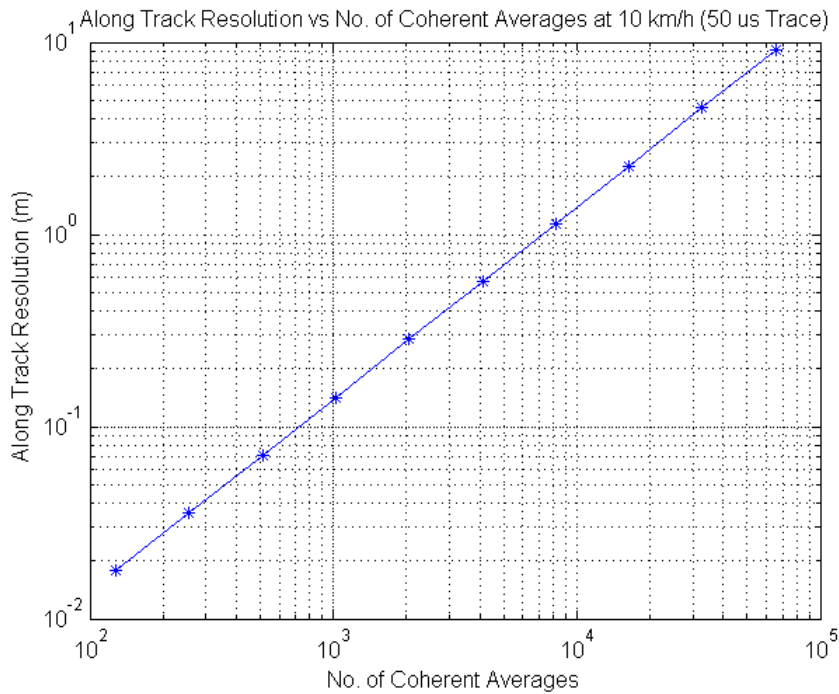


Figure 2-9 Along-Track Resolution vs. No. of Coherent Averages for Deep Ice

As the number of coherent averages plays an important role in the calculation of loop sensitivity, it is a trade-off between keeping SNR high and getting reasonable along-track resolution when it comes to moving radar system. Otherwise, along-track resolution can be improved by decreasing speed, although this means longer time to collect an equivalent amount of data and/or less data collected.

Field measurements can be initiated by first setting a large number of coherent averages, so that the chirp can be captured and recovered through the matched filter. As decreasing the number of coherent averages will lower the SNR, a trade-off has to be made. When placing the system at a fixed location, if the matched-filtered chirp is clear enough and identical to the noise floor, the number of coherent averages can be decreased to increase the along-track resolution. After decreasing the number of coherent averages, if the matched-filtered chirp is still identical, detection while moving can begin.

Due to characteristics of ice sheets such as stratification, porosity, water content, and bedrock rough surfaces, degradation will vary. So parameter-tuning will also be different. Most

probably, more coherent averages will be needed, considering the theoretical received power is calculated under ideal conditions, without taking into account characteristics such as stratification or water content.

2.7 Data from Antarctica

During the field test in Antarctica in January, 2014, the PXI-based Ice Radar was used. Important data were collected. Figure 2-10 shows one example of a captured single trace. A chirp can be discerned from the bottom trace at around 11 μs . The accurate time the chirp started to be captured can be identified through the matched filtered trace (Figure 2-11).

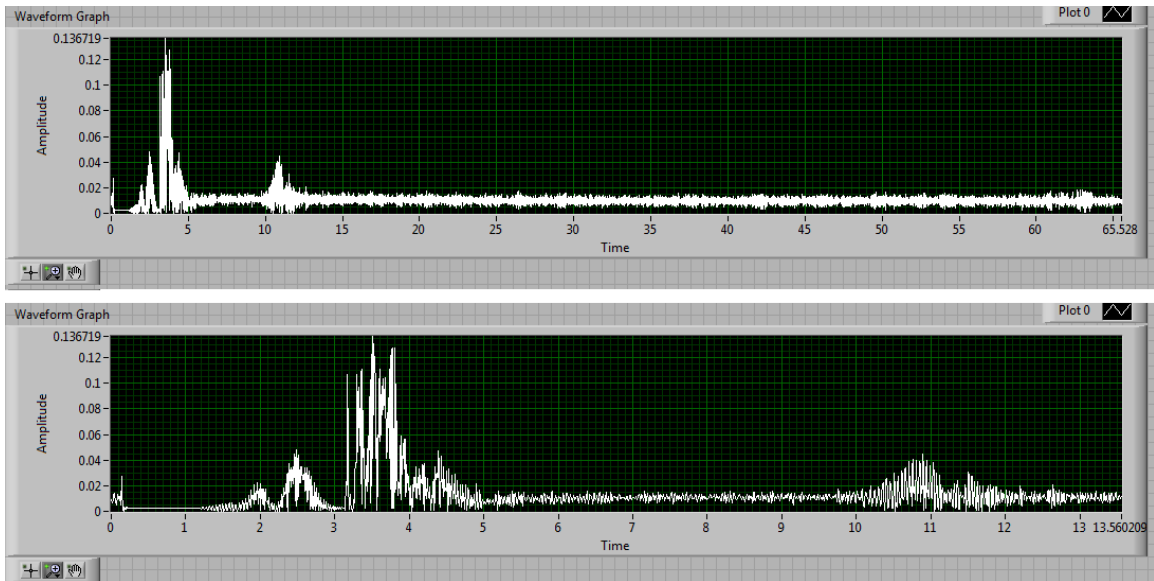


Figure 2-10 Waveform of Captured Trace from PXI-based Ice Radar

Figure 2-11 shows a clear peak at around 10 μs , with very good SNR. The accurate time delay is shown at the right side as 9.688 μs . This result shows that the PXI-based Ice Radar was functioning very well and the measurement was successfully obtained.

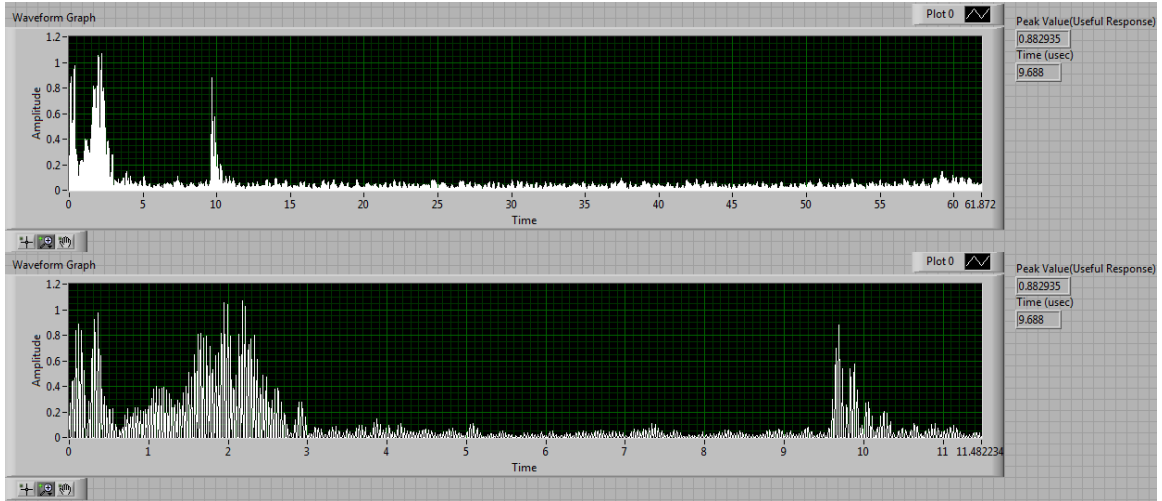


Figure 2-11 Waveform of Matched Filtered Trace from PXI-based Ice Radar

So based on the success of the PXI-based Ice Radar system, the USRP-based radar has been designed and developed.

Chapter 3 System Design

As stated in Chapter 1, the initial design goal for the Ice Radar is to build an ice-penetrating radar that is compact, portable, flexible, and adaptable to future requirements. This USRP-based Ice Radar uses the USRP instead of the PXI platform to achieve better flexibility, portability, and adaptability. An external FPGA is required for the digital I/O, clock signal, and synchronization trigger. All COTS components are able to function at temperatures as low as $-30\text{ }^{\circ}\text{C}$. Although the operating temperature range for the USRP is specified to be between 0 and $45\text{ }^{\circ}\text{C}$, the Ice Radar is placed in an insulated aluminum box that remains above $0\text{ }^{\circ}\text{C}$ due to the heat generated by the power amplifier. In this chapter, individual components and the various parts of the radar will be introduced and the interactions among them will be presented.

The block diagram of the Ice Radar system is shown in Figure 3-1 and the parameters driving the system design are listed in Table 3-1.

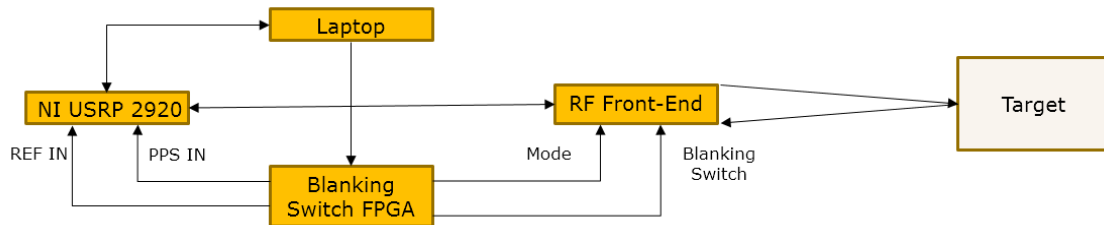


Figure 3-1 Block Diagram of the Ice Radar System

Table 3-1 Ice Radar System Parameters

Parameter	Parameter Values
Baseband Frequency	5–10 MHz
Sampling Rate	20 MHz
Carrier Frequency	142.5 MHz
Chirp Duration	1 μs , 3 μs , 5 μs
Trace Duration	50 μs , 25 μs , 10 μs
Peak Transmit Power	20 W
Pulse Repetition Frequency	> 20 kHz

3.1 USRP and Laptop

Used in both the Systems Design Laboratory (SDL) and Student Space Programs Laboratory (SSPL), the USRP is a software-defined-radio device for both research and education. LabVIEW is also used as a programming language in these two laboratories, and all required packages are available, i.e., NI-USRP, NI-VISA, and NI Modulation Toolkits. This equips the USRP with the ability to be flexible and adaptable to future system requirements. The USRP is more compact than the PXI chassis—the USRP is about 1/10 the size of the PXI chassis. As the USRP uses fewer external cable connections, it is more portable and easier to integrate.

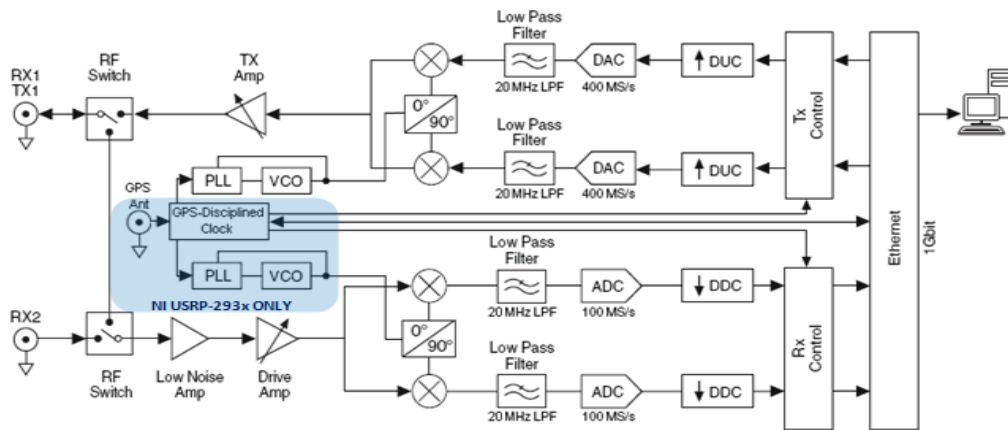


Figure 3-2 NI USRP 2920 System Block Diagram [29]

Figure 3-2 provides the block diagram of NI USRP 2920, which is comprised of a motherboard and daughterboard and optional GPS module. The NI USRP 2920 is equipped with the Xilinx Spartan 3A-DSP3400 FPGA on the motherboard, and the WBX 50-2200MHz RX/TX as daughterboard (Figure 3-3).

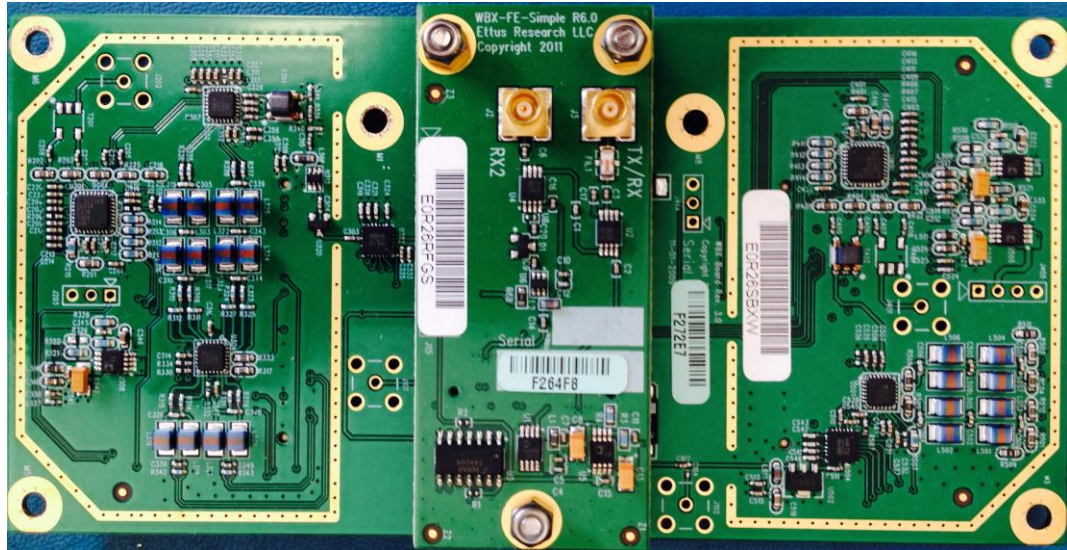


Figure 3-3 USRP 2920 Daughterboard WBX

The WBX daughterboard has two SMA ports, one of which can be configured as either TX or RX from within LabVIEW. The other SMA port works as RX only. Both ports can handle signals with frequencies ranging from 50 MHz to 2.2 GHz, and a maximum I/Q sampling rate of 25 MS/s for a 16-bit sample width. For the TX, the maximum output power ranges from 17 to 20 dBm over the frequency range from 50 MHz to 1.2 GHz, and the gain ranges from 0 to 31 dB in 1-dB steps. As the maximum output power after gain settings varies with frequency band, the gain parameter has to be set by measuring the actual output, such as with a calibrated spectrum analyzer. The maximum input power to the RX section is 0 dBm; due to this limit, a 0-dBm limiter is included in the RF front-end box to prevent excessive power going into the RX. The gain range for the RX is 0 to 31.5 dB, in steps of 0.5 dB. The noise figure for the RX is from 5 to 7 dB. As it is at the end of the whole receiver path, according to [30], this impact on overall noise figure will be minimal.

The motherboard is illustrated in Figure 3-4. The motherboard contains a Xilinx FPGA, two 100-MHz 14-bit ADCs, and two 400-MS/s 16-bit DACs. One Gigabit Ethernet interface is provided for communication with a computer. A MIMO interface is also provided, allowing a maximum of two USRP units to be connected, such as required for a 2x2 MIMO configuration.

There are also inputs for external pulse-per-second (PPS) and clock references, to allow an external clock signal to be used as an external synchronization trigger for TX and RX. In this project, a 10-MHz reference signal is output from the external blanking switch FPGA (referred to herein as the “external FPGA”) and input to the REF IN port on the USRP, and a square wave trigger applied to the PPS IN to trigger the 2-s delay before synchronization. Rationale for and the methods of generating these two signals are discussed in Section 3.3.



Figure 3-4 USRP 2920 Motherboard with Xilinx Spartan 3A-DSP3400 FPGA

The USRP works by up/down-sampling the signals in the FPGA, but the attached computer does all the signal configuration and calculation; hence, a high-performance controlling computer is required to achieve maximum bandwidth and performance. Although the maximum I/Q sampling rate is 25 MS/s for a 16-bit sample width, the actual sampling rate is highly dependent on the performance of the controlling computer. As a high-performance laptop can help achieve 20 MS/s sampling rate, this was ultimately selected as the sampling rate of this Ice Radar. To satisfy the Nyquist Sampling Theorem, the chirp frequency is set to be 5 to 10 MHz. In addition,

to match the PXI-based Ice Radar in frequency range, the center frequency is set to be 150 MHz, which means the carrier frequency is 142.5 MHz.

The laptop used for USRP-based Ice Radar system development is a MacBook Pro. The CPU is a quad-core Intel Core I7-3840QM with processor speed of 2.8 GHz. It has 16 GB of 1600-MHz DDR3L onboard RAM, a 768-GB solid state hard drive, Intel HD Graphics 4000 graphics card, and a Gigabit network adapter. The USRP was connected to the laptop via a CAT-5 Ethernet cable, through a Thunderbolt to Gigabit Ethernet adapter. This computer configuration allowed 20 MS/s to be processed. In [31], a MXE 5302 single-board computer was used which could achieve 20 MS/s sampling frequency with the USRP 2920. As the sampling frequency is highly dependent on the laptop performance, future work will require a laptop with equal or better CPU, solid state hard drive, and a Gigabit or even 10 Gigabit network adapter. If using the NI USRP RIO, the limiting factor will be the communication between controlling computer and USRP. In this case, a PCI Express card will be needed.

3.2 TX & RX Front-End Paths

Details of RF front-end box design have been elaborated in [14]. As mixers and low noise amplifiers have been built into the USRP daughterboard, the up-conversion module is not required in the USRP-based Ice Radar RF front-end path. Also, since the TX port of the USRP can generate up to 17 dBm output power, no additional low power boost amplifier is needed before the power amplifier. As was discussed in Section 2.3, the max input of the power amplifier is 0 dBm, and to output 20 W signal power, the input to the power amplifier is supposed to be -7 dBm. The output from TX port of USRP is specified to be 0 dBm. This output is reasonable because the overall insertion loss of the following components is less than 7 dB. So by adding a proper attenuator, the -7 dBm input to the power amplifier is easy to achieve. The design is discussed in Section 3.2.1. The frequency range of the baseband chirp is from 5 to 10 MHz, and the carrier frequency is 142.5 MHz, which gives the USRP-based radar the same center frequency as the PXI-based radar.

3.2.1 TX Front-End Path

Figure 3-5 shows a spectrum analyzer plot of the transmitted signal, clearly showing the frequency components of the up-converted chirp, carrier, and aliased signals. A BPF with 5-MHz bandwidth and 150-MHz center frequency is required in between the USRP TX port and the power amplifier to remove the carrier waveform such that the RX front-end and USRP are not damaged. To mitigate VSWR and improve component performance [14], an attenuator is added between the BPF and power amplifier.

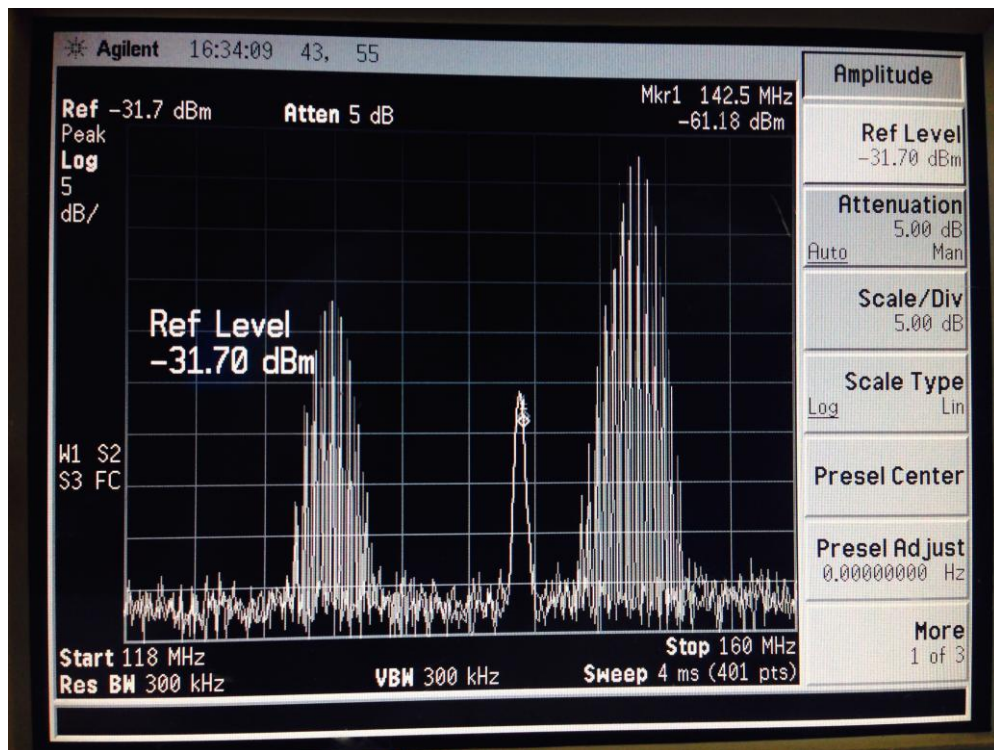


Figure 3-5 Power Spectrum of Signal Transmitted from USRP

There are four SPDT switches in the RF Front-End paths, two of which are for mode selection, whereas the other two are for blanking the high power signal such that it is not directly fed into the RX path. The switch in the TX path selects between glacier mode, which is for use in the field, and the calibrate mode, which is for use during system test before being connecting to the power amplifier. The gain of the power amplifier is 50 dB at 100 MHz and the maximum

input power that will not cause damage is 0 dBm. Hence, to obtain 20-W output, -7 dBm input is needed. The TX path loss is 7.2 dB, so around 0 dBm is output from USRP TX end.

The switch is controlled by a TTL signal, with TTL high controlling Port 1 closed and Port 2 open, and TTL low controlling Port 1 open and Port 2 closed. In the calibrate mode, a -50 -dBm signal is output from the USRP, and after going through Port 2 of the switch, it is directed to two 20-dB attenuators, causing 96-dB attenuation to the signal. In the glacier mode, a 0-dBm signal is output from the USRP, and at the other end of the TX path, an antenna is connected to the power amplifier.

3.2.2 RX Front-End Path

The RX path block diagram is shown in Figure 3-7. Switch SPDT_2 also is used for mode selection. The design choice of a switch instead of a directional coupler is based on several tests in which it was determined that a directional coupler caused unstable chirp signals. In either glacier or calibrate mode, the signal feeds in through the first switch, then through a BPF that filters out undesired frequency components outside the range of 147.5 to 152.5 MHz. Placing the BPF right before the LNA helps ensure that high frequency components are filtered out without causing reflections within the amplifier [14][30]. When the blanking switches are not engaged, the reflected signals go through three amplifiers, two open-path switches, and two 3-dB attenuators, for a total path gain of 90 dB. Attenuators between amplifiers serve the same function as the one in the TX path. Finally, as amplifiers generate and amplify noise throughout the amplifier frequency range, another BPF is connected to block noise that is not within the BPF pass band, which helps both improve SNR, and to ensure that no destructive signals feed into the USRP. The 0-dBm power limiter is the final element in the RX chain, and is able to withstand a maximum of 10-W average power and 100-W impulse pulse (with duty cycle of 10%). It was designed for use in a network analyzer, so it has high stability and good performance. As discussed in Section 3.5, signals arriving directly from the TX antenna to the RX antenna, or reflections from ice sheet surface will be lower than 5 dBm. This input to the RX path will cause

saturation to the amplifier output. After going through the three amplifiers in the RX front-end path, the saturated signal will be higher than 0 dBm, which means it is higher than the USRP input power limit. The existence of the power limiter enables continual saturation to the signals, so that the USRP is not damaged.

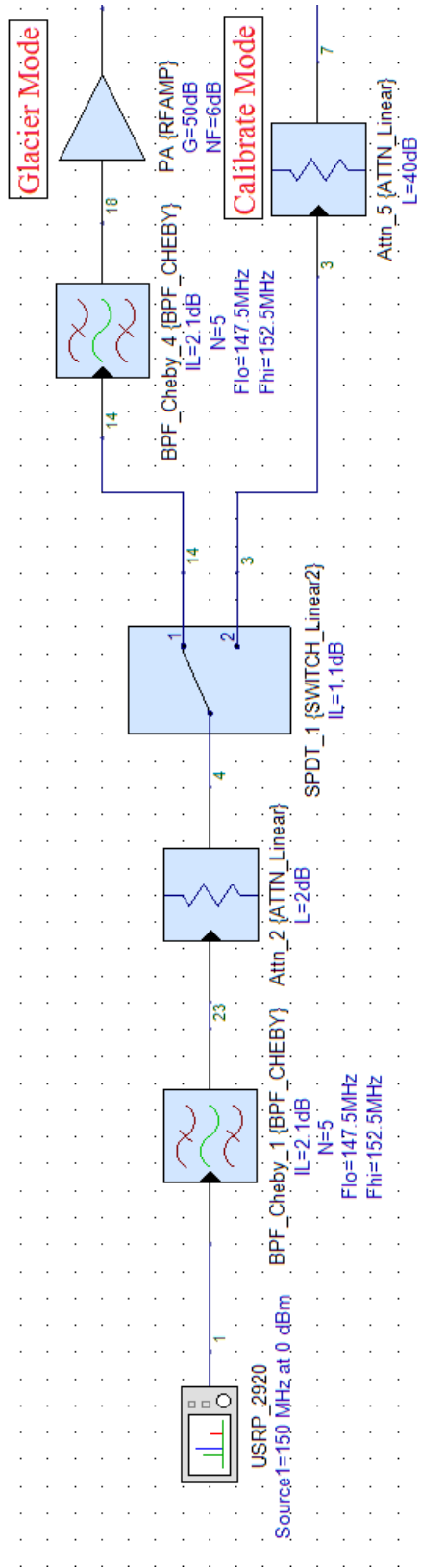


Figure 3-6 TX Front-End Path Block Diagram

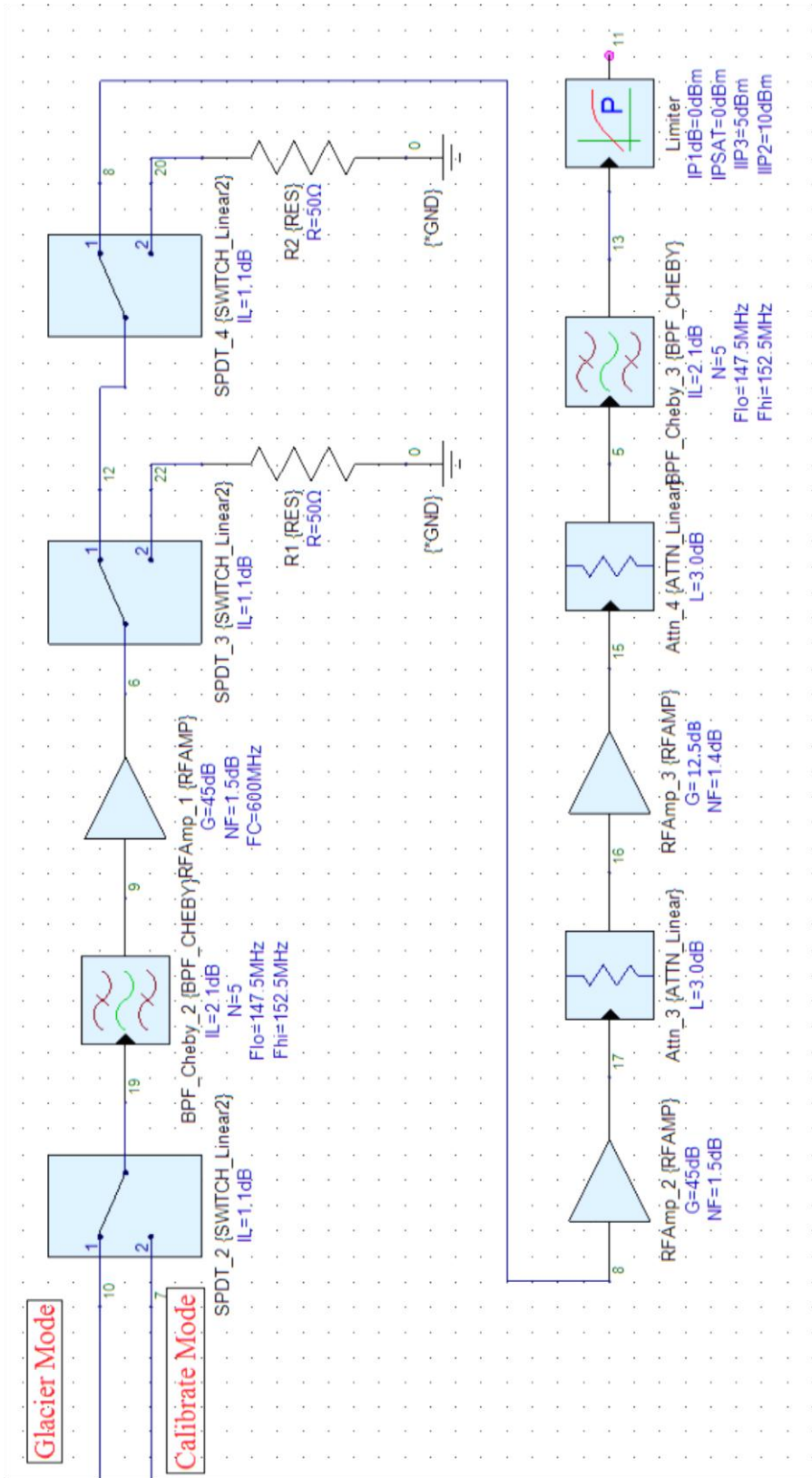


Figure 3-7 RX Front-End Path Block Diagram

3.3 Blanking Switch

As shown in Figure 3-7 and discussed in Section 3.2.1, the blanking switch module is composed of four parts: two SPDT switches, one power combiner, and one external FPGA. The design uses the Cyclone IV FPGA, and programmed in Verilog. Ports 2 of both of these two switches are connected to a power combiner into a 0.25-W terminator. Port 1 of the left switch is connected to the input of the right switch, whereas Port 1 of the right switch is connected to the rest of the receiver path. Basically, when the USRP-based Ice Radar starts working, a code is sent through a USB cable to the external FPGA, the external FPGA waits 2 s until the USRP starts running, and then starts sending the required TTL signals to the switches. Simultaneously, a 10-MHz clock signal is output to the USRP as a common reference clock, and a trigger PPS is sent to the USRP for synchronization.

The design decision to use two switches instead of one was based on leakage consideration. This design ensures that, even if there is leakage in one switch, the other will ensure the signal flows to the terminator. Also, if one is damaged, the other makes sure no high power goes through the receiver path and into the USRP.

The external FPGA works at 6 V DC, with one USB Standard-B receptacle. A USB Standard-A to USB Standard-B cable connects the laptop and the external FPGA. An unsigned 8-bit code is sent to indicate the messages as described in Table 3-2.

Table 3-2 USRP-External FPGA Communication Message Structure

Bit location*	Combination	Representation
7	0	External FPGA idle for data acquisition
	1	External FPGA running
6, 5, 4	1 0 0	50- μ s trace for deep ice detection
	0 1 0	25- μ s trace for middle-depth ice detection
	0 0 1	10- μ s trace for shallow ice detection
3	0	Glacier mode
	1	Calibrate mode
2, 1, 0	1 0 0	Chirp length of 5 μ s
	0 1 0	Chirp length of 3 μ s
	0 0 1	Chirp length of 1 μ s

*bit 7 represents MSB, 0 represents LSB

The external FPGA works with an internal reference clock set at 100 MHz. When a message is received via the 8-bit protocol described above, a 10-MHz reference clock starts to be outputted. The reason the external reference clock is utilized is because separate clock signals will cause a phase shift between the chirp trace and the blanking switch trace. Simultaneously, a 500-Hz squarewave is output to the USRP, with initial state low. This initialization leaves a 1-ms delay before the first rising edge, which makes sure that the delay caused by configuration in the USRP and communications between the laptop and the USRP will not cause the USRP to miss the first rising edge of the squarewave. At the first rising edge, a counter starts to count to 2×10^8 before sending the first TTL signal to the blanking switches, which means it is sent 2 s after the first rising edge. The 2-s delay is set such that the external FPGA is synchronized with the 2-s USRP onboard delay required by internal TX/RX synchronization. Trace and chirp lengths are defined according to the protocol information.

With respect to updates in the blanking switch, in the PXI-based Ice Radar, the blanking switch module would not work in the calibrate mode, whereas in USRP-based version, it will work in both calibrate and glacier modes. This ensures that the blanking switch module can be tested. One example of the test is described here: In the calibrate mode, if we use the 3- μ s chirp

mode, we set the chirp delay as 0, 1.5, and 10 μs . If there were no delay, the chirp cannot be identified between 0 μs and 3 μs ; with a 1.5- μs delay, only a half chirp is seen from 1.5 μs to 3 μs ; and with a 10- μs delay, a whole chirp shows up from 10 μs to 13 μs , indicating that the blanking switch module is functioning. In this manner, before real field testing occurs, a test in the calibrate mode can help to identify whether the system, and especially the blanking switch, is working properly. Once a clear chirp is identified from 0 to 1/3/5 μs (chirp duration), the system will not block the direct arrival chirps when in the glacier mode. In this case, troubleshooting should be carried out and the system should not be used in the field test until the blanking switch can block the chirp at the beginning of the trace.

3.4 Chirp Signal and Antennas

During the winter of 2013, field data were collected by Prof. Anandakrishnan in Antarctica using the PXI-based Ice Radar. The recovered plots, especially for the matched-filtered traces, are discontinuous. To understand the cause of this, we were able to simulate the results, as shown in Figure 3-8. The ups and downs in the matched filtered trace are caused by the fact that the chirp signal is sinusoidal with linearly increasing frequency. The matched filters apply a cross-correlation algorithm, with the highest cross-correlation value representing the time when the radar starts capturing the reflected chirp.

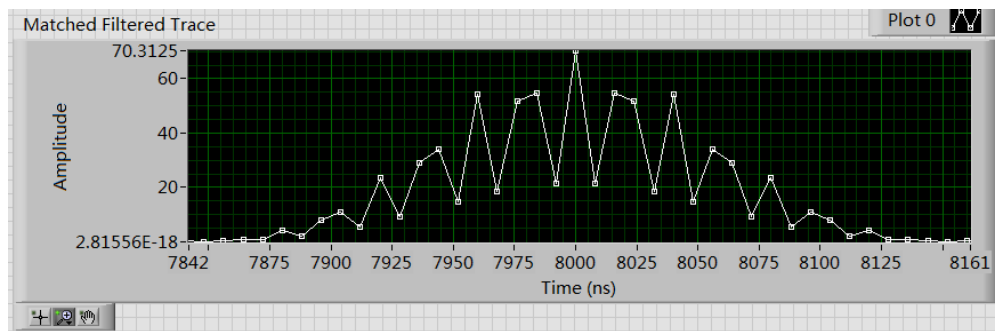


Figure 3-8 Simulation of Matched-Filtered Trace for PXI-based Ice Radar

In the USRP-based Ice Radar, an I/Q modulated chirp signal is generated instead, from which a smooth cross-correlation curve can be obtained. Similar curves are provided in

Section 2.5, while single chirp matched-filtered result is given in Figure 3-9. From this plot, we can see that the curve is smooth and, hence, the peak is easier to identify.

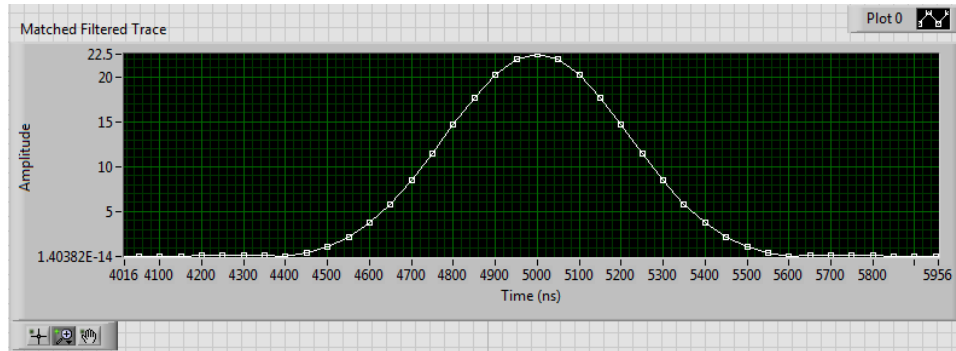


Figure 3-9 Simulation of Matched-Filtered Trace for USRP-based Ice Radar

When IQ data are to be sent through an I/Q modulator, the in-phase data are mixed with the carrier, whereas the quadrature data are mixed with the carrier with a 90° phase delay (see Figure 3-11). In equation form and with reference to Figure 3-10, the RF waveform obtained is

$$\begin{aligned} y_{\text{mod}} &= M(t) \times \cos(2\pi f_c t) \cos(\phi(t)) - M(t) \times \sin(2\pi f_c t) \sin(\phi(t)) \\ &= M(t) \times \cos(2\pi f_c t + \phi(t)) \end{aligned} \quad (3.1)$$

In this project, an I/Q chirp is to be generated. For a single chirp, the expression is

$$y = M(t) \times \sin\left(2\pi f_0 t + 2\pi \frac{f_1 - f_0}{2\tau} t^2 + \phi\right), \quad (3.2)$$

where f_0 is the chirp start frequency, f_1 is the chirp stop frequency, τ is the chirp duration, and ϕ is the initial phase of the chirp.

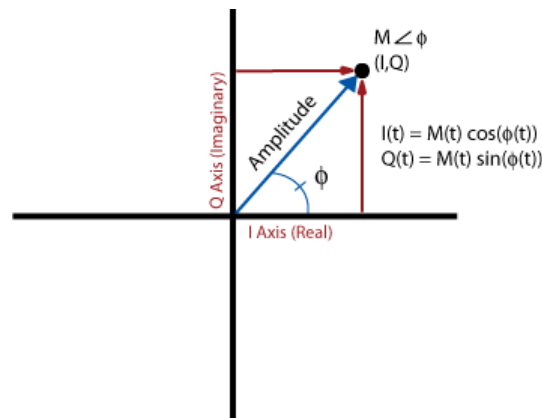


Figure 3-10 I and Q values of I/Q Modulation [32]

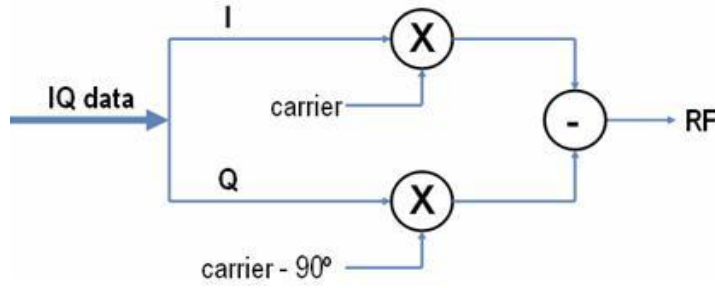


Figure 3-11 I/Q Modulator [33]

The I/Q chirp is generated by defining the in-phase values to be a chirp with 90° phase, while the quadrature values a chirp with 0° phase. This can be expressed as:

$$\begin{aligned}
 y &= M(t) \times \cos(2\pi f_c t) \sin\left(2\pi f_0 t + 2\pi \frac{f_1 - f_0}{2\tau} t^2 + \frac{\pi}{2}\right) \\
 &\quad - M(t) \times \sin(2\pi f_c t) \sin\left(2\pi f_0 t + 2\pi \frac{f_1 - f_0}{2\tau} t^2\right) \\
 &= M(t) \times \cos\left(2\pi f_c t + 2\pi f_0 t + 2\pi \frac{f_1 - f_0}{2\tau} t^2\right) \\
 &= M(t) \times \cos\left(2\pi(f_c + f_0)t + 2\pi \frac{(f_c + f_1) - (f_c + f_0)}{2\tau} t^2\right). \quad (3.3)
 \end{aligned}$$

Thus, the I/Q modulated chirp can be expressed as a chirp with frequency range from $f_c + f_0$ to $f_c + f_1$ and amplitude of $M(t)$. As the modulated signal is still a linearly polarized signal, the log-periodic antennas that were applied for PXI-based Ice Radar can be directly applied to this project.

3.5 Maximum Direct Input Power

Considering that the maximum input signal power is 13 dBm for the AU-1027 amplifier, maximum direct input power needs to be calculated to ensure no saturation occurs, and no damage is caused to the components. Detailed input power calculation can be found in [14].

3.5.1 Direct Arrival Power

As is discussed in [14], the direct arrival power is the power that directly couples from the TX antenna to the RX antenna, and is calculated by knowing the transmitted power, TX and RX radiation patterns, and loss in the medium, i.e.,

$$P_r = \frac{P_t G_{t,\varphi1} G_{r,\varphi2}}{L_{\text{air}}}. \quad (3.4)$$

For this system, P_t is 43 dBm and $G_{t,\varphi1}$ and $G_{r,\varphi2}$ are -30 dBi. As the separation between the two antennas is only 4 m, propagation loss in the air can be ignored (i.e., $L_{\text{air}} = 1$). In our case, the direct arrival power is calculated to be a maximum of -17 dBm. As the maximum input power for the AU-1027 amplifier is 13 dBm, and 1-dB compression power is 12 dBm, the direct arrival power is much smaller. Also, the blanking switch will block most power and the performance of the rest of the RX path will not be affected.

3.5.2 Air–Snow Reflection Arrival Power

To calculate the air–snow reflection arrival power, we use

$$P_r = \frac{P_t G_{t,\varphi1} G_{r,\varphi2} \Gamma}{L_{\text{air}}}, \quad (3.5)$$

where Γ is the reflection coefficient, calculated by

$$\Gamma = \left| \frac{\sqrt{\varepsilon_{\text{air}}} - \sqrt{\varepsilon_{\text{snow}}}}{\sqrt{\varepsilon_{\text{air}}} + \sqrt{\varepsilon_{\text{snow}}}} \right|^2, \quad (3.6)$$

where ε_{air} and $\varepsilon_{\text{snow}}$ are the permittivities of air and snow, respectively. Here, 1 and 1.5 are applied as relative permittivities of air and snow [14]. This yields a reflection coefficient of -20 dB.

As the distance between the antennas is 4 m and the distance between the phase centers of antennas to the ice surface is around 1.36 m, the incidence angle can be calculated as 60° , which means $G_{t,\varphi1}$ and $G_{r,\varphi2}$ are -9 dB. The received power is then 5 dBm, which is also less than the upper limit of 13 dBm.

3.6 SystemVUE Simulations

The RF front-end paths can be divided into two sub-paths based on the selection between glacier and calibrate modes. In order to observe and check the channel power along these two paths, Agilent SystemVUE was used.

3.6.1 Simulation of Glacier Mode

In this mode, a 0-dBm signal is generated by the USRP, and the output power of the power amplifier is 20 W. In the simulation, a 176-dB attenuation is added between the power amplifier and the receiver switch to account for the attenuation due to the ice sheet and bedrock reflection, which was calculated in Chapter 2. The simulation result shows that when 0 dBm is output from the USRP, a 42.0 dBm signal is output from the power amplifier, and the USRP receiver sees an input of -15.45 dBm, which is below the RX input limit of 0 dBm. Figure 3-12 shows the SystemVUE simulation of power level for the glacier mode RF path. Adjustments can be carried out in the field if needed by changing the RX gain in USRP using the LabVIEW front panel.

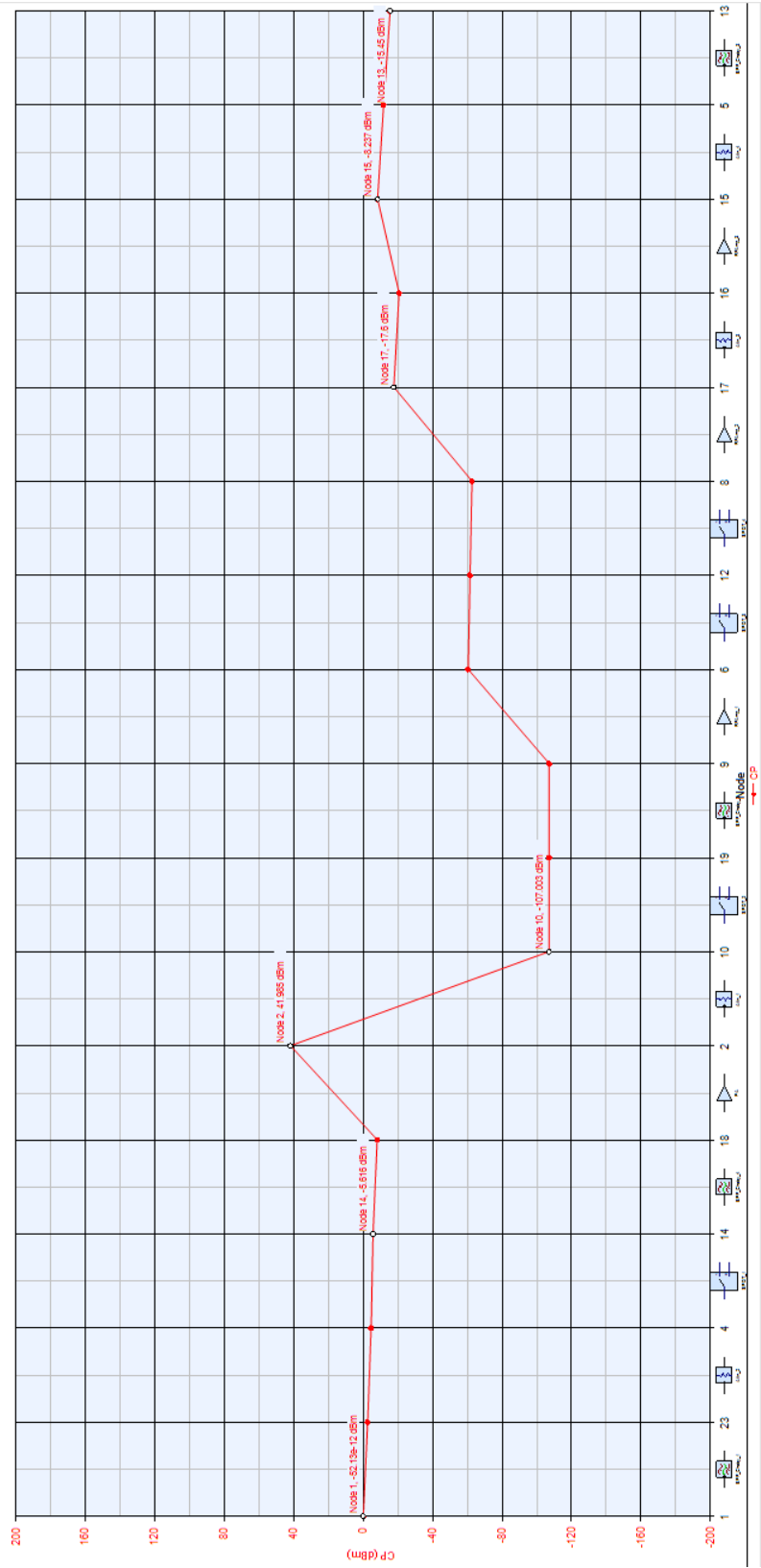


Figure 3-12 Simulation of Channel Power along Glacier Mode Path

3.6.2 Simulation of Calibrate Mode

In the calibrate mode, a -50 -dBm chirp is output and then sent through Port 2 of the switch in the TX path, which then includes two 20-dB attenuators. The TX signal power and the attenuator after the switch are different from those used in the PXI-based Ice Radar, in that the step attenuator is removed, the gain of amplifiers in the RX path is increased, and the allowable RX signal power is lower. When the -50 -dBm signal is transmitted, the receiver path receives -98.5 dBm and, at the USRP receiver, the final received power is -8.2 dBm, which is lower than the maximum input power limit of USRP.

In the calibrate mode, the TX gain in the USRP should be set to 0, considering the output power has to be -50 dBm, whereas the RX gain in USRP can be adjusted for calibration, but the input power of USRP must remain less than 0 dBm.



Figure 3-13 Simulation of Channel Power along Calibrate Mode Path

3.7 Programming

The USRP-based Ice Radar system is programmed using LabVIEW. The following additional packages are used: NI USRP toolkit, which is used for programming the USRP, including parameter configuration, trigger configuration, TX/RX synchronization, session opening/closing, and data transmission/acquisition; NI VISA is used for USB communications with both the U-blox GPS and external FPGA; and NI MathScript RT module and NI Modulation toolkit are needed, which are complements of the NI USRP toolkit. Additionally, u-center is installed to capture GPS information, and Verilog is used to program the external FPGA.

The flowchart presented in Figure 3-14 helps to explain the connections and the communication paths between the laptop, external FPGA, and USRP. In contrast to the PXI-based Ice Radar, which performed the matched filtering in the FlexRIO, the USRP-based Ice Radar performs this matched filtering on the laptop. Also, although band pass filtering was employed in the FlexRIO, it is not employed in the LabVIEW program for the USRP-based Ice Radar. This is because it will increase the overall processing time, causing delay to receiving data from the USRP, which can cause an underflow error.

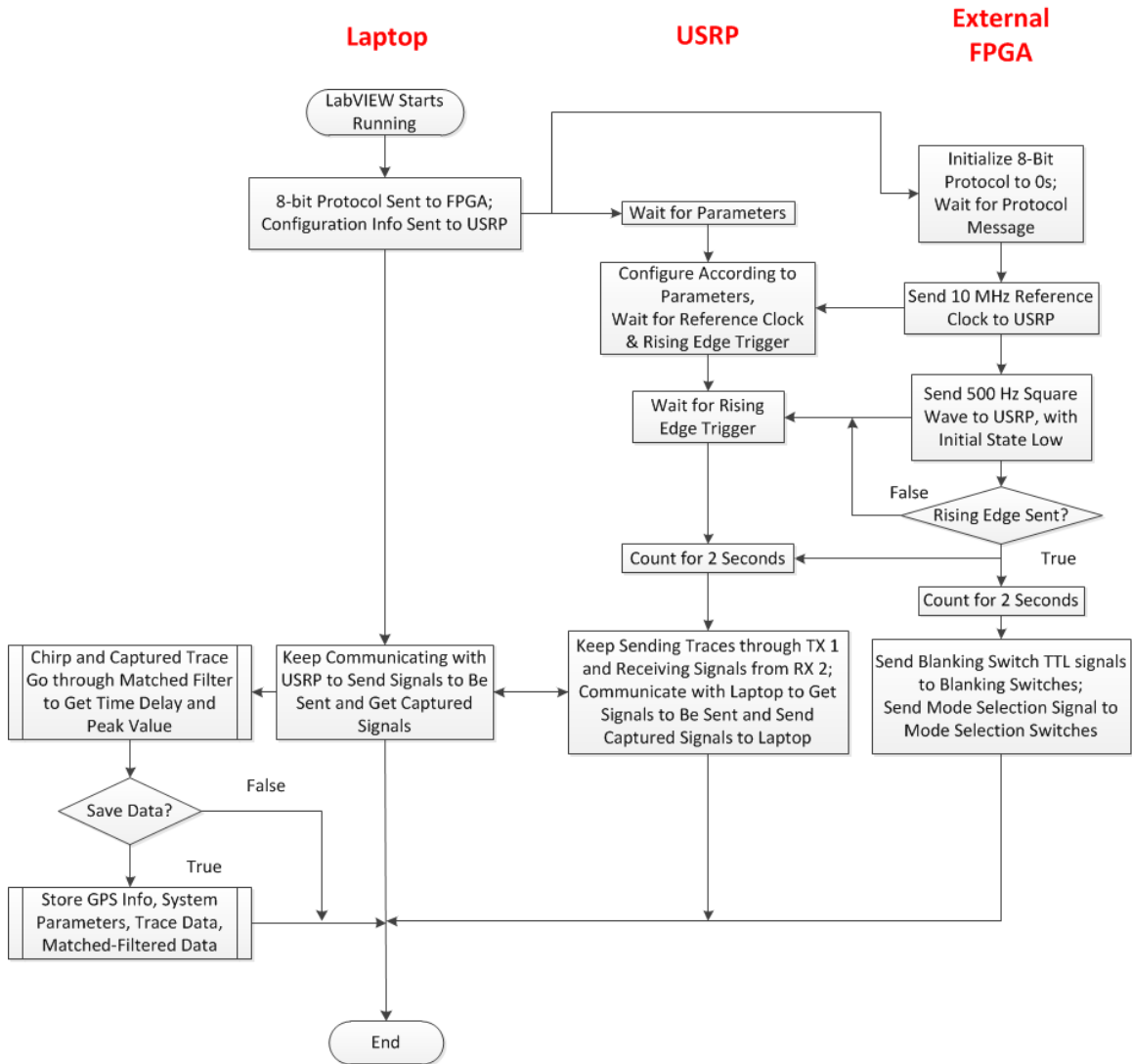


Figure 3-14 Flowchart of the Ice Radar System

The process after system starts running is as follows:

1. After LabVIEW starts running, the file path for saving data files is selected. Parameters are passed to the niUSRP Configure Signal VIs, after which the I/Q chirp is generated according to the coerced I/Q rate and the defined time duration. A Hanning window is applied to the real and imaginary parts of the chirp, generating a chirp signal with its amplitude smoothly increasing and decreasing. The entire trace is generated: for the glacier mode zeroes are padded to the chirp, whereas in the calibrate mode zeroes are

padding to the front and end of the chirp according to the defined delay. At the same time, the 8-bit protocol message to be transmitted to the external FPGA is generated.

2. The start trigger time is added to the niUSRP Configure Trigger VIs for both TX and RX codes. The TX start trigger time is defined as 2 s. As there is a 1.85- μ s delay in the RX, the start trigger time for RX is set to be 1.85 μ s later than the TX start trigger time. The reference clock source and trigger type are also defined after the trigger time configuration. Then the time stamp is sent through the Ethernet cable to the USRP. At the same time, the pre-defined 8-bit protocol message is sent to the external FPGA, and it starts its program. The USRP waits until the rising trigger edge is sent to the PPS IN.
3. After the start trigger time, the data transmission loop and data acquisition start to work. To avoid underflow error, multiple traces to be transmitted were concatenated into a single long trace. At the same time, in the data acquisition loop, for each trace, the number of samples is the same as that of the trace before concatenation.
4. The data acquisition loop works on sample acquisition, coherent averaging, matched filtering, and data storage.
5. The system continues on until the stop button is pressed, or an error occurs.

Before the system starts, all unnecessary software running on the laptop should be shut down to save memory for LabVIEW. Also, as the network adapter is used to communicate with the USRP, no other network traffic should occur, otherwise an underflow error will occur.

3.7.1 LabVIEW Front Panel

LabVIEW is employed not only as a programming environment, but also as the system's graphical user interface (GUI). There are three sections of the front panel (Figure 3-15):

1. Signal and USRP configurations and error information. They are separated using three tabs;
2. Averaged trace and matched-filtered signal displays. They are displayed on the right side of the panel, and the sample delay is displayed right to the matched-filtered signal display; and
3. GPS information and file paths. These indicate the file paths for saving information on system configuration, captured data, and matched-filtered data.

The signal configuration tab is used for glacier/calibrate mode selection, chirp duration determination, ice depth selection, defining the number of coherent averages, and chirp frequency definition. Also, trace delay in the calibrate mode is defined, and the I/Os for the GPS and external FPGA are also defined here. The “Start Recording” button determines whether or not captured data is to be stored. The trace to be transmitted will also be displayed in this tab.

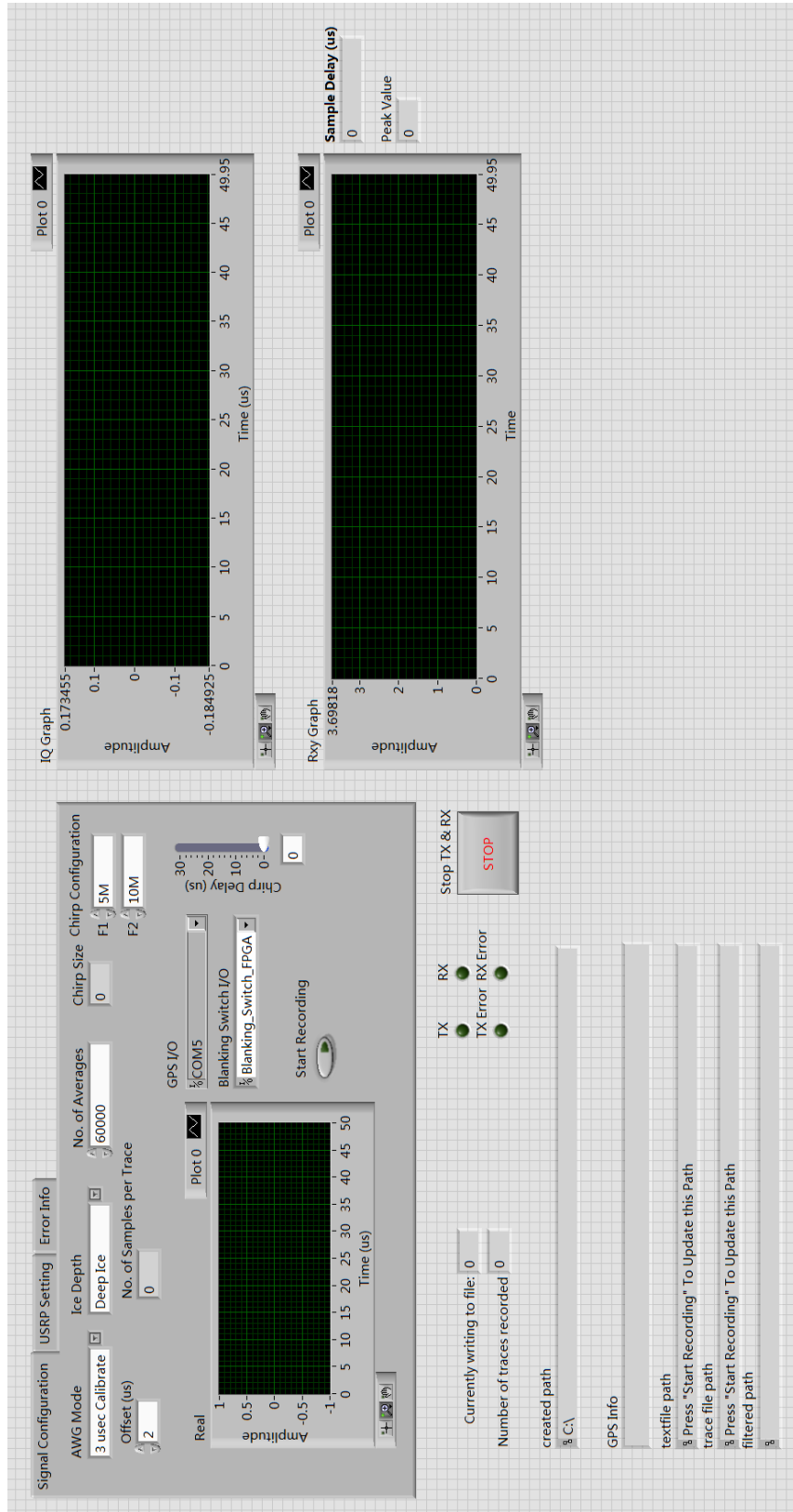


Figure 3-15 LabVIEW Front Panel of Ice Radar System

The USRP Setting tab (Figure 3-16) includes all the parameters related to USRP, including device IP address, sampling rate, carrier frequency, TX and RX gains, and TX/RX ports. The coerced parameters are also provided in this tab.

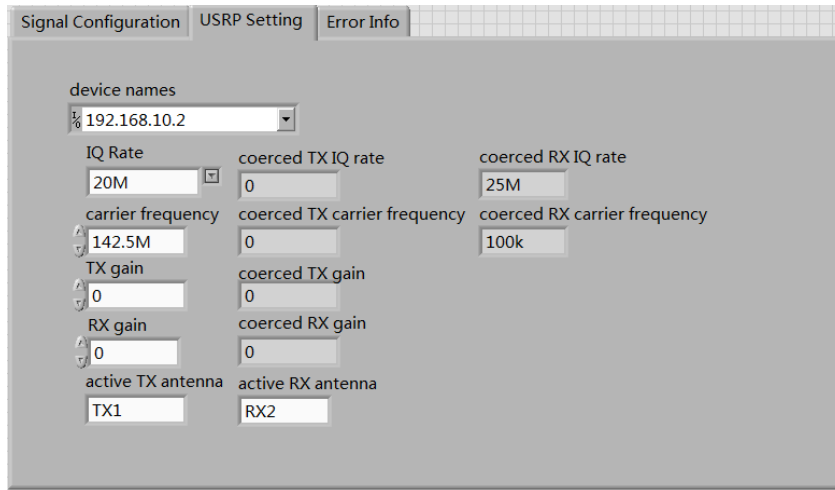


Figure 3-16 USRP Setting Tab

All the parameters are able to be changed based on field test results. To make sure no high power goes through the band pass filters, when changing chirp frequency range, calculations are needed to ensure carrier frequency component is safely blocked.

The “IQ Graph” displays the real captured traces, with the white curve representing real part of the trace and red curve representing imaginary part. The “Rxy Graph” displays the absolute value of the matched filtered traces, which will show peak time and value.

TX and RX LED lights indicate whether the data transmission and data acquisition loops are working. If the TX LED lights later than the RX LED, or only one lights up when the system is running, an error occurs. The system should be stopped and checked for problems.

3.7.2 Waveform Generation

As stated previously, the waveform to be transmitted is composed of the chirp and zero padding. The baseband chirp signal frequency range is from 5 to 10 MHz. The chirp signal generated here is from a self-programmed chirp pattern generation VI, which adds the phase

parameter. The G code presented in Figure 3-17 is the coded version of the chirp signal given in Eqn. (3.7), which is the digital form of Eqn. , (3.2):

$$y = A \times \sin \left[\left(\frac{2\pi(f_2 - f_1)}{2n} i + 2\pi f_1 \right) i + \phi \right], \quad (3.7)$$

where f_1 is the beginning frequency in normalized units of cycles/sample, f_2 is the ending frequency in normalized units of cycles/sample, and n is the number of samples. When using a 20-MHz sampling rate, chirps of 1, 3 and 5 μ s have 20, 60, and 100 samples, respectively. Using the chirp pattern generator, the entire trace is generated as shown in Figure 3-18.

A selector VI is applied to determine whether delay is added before the chirp based on calibrate/glacier mode selection. Trace length is chosen from 10, 25, and 50 μ s, thus the pulse repetition frequency (PRF) can be 100, 40, and 20 kHz, respectively.

3.7.3 TX/RX and External FPGA Synchronization

As at least 2 s are needed to synchronize TX and RX, a trigger is needed to initialize the synchronization. This trigger can be from either an internal or an external PPS edge. Also, to make sure the external FPGA is synchronized with TX and RX, an external rising edge is required, accompanied by external clock source, as the clock signals on the USRP and external FPGA are not in phase.

As shown in Figure 3-19, in the Flat Sequence Structure, the 8-bit protocol message and initial timestamp are transmitted at the same time. Immediately following receipt of these, the external FPGA generates a 500-Hz square wave with initial state low. This method overcomes the communication delay between laptop and the USRP caused by the non-deterministic communication over Ethernet. This method provides accurate synchronization, as shown in Figure 3-20.

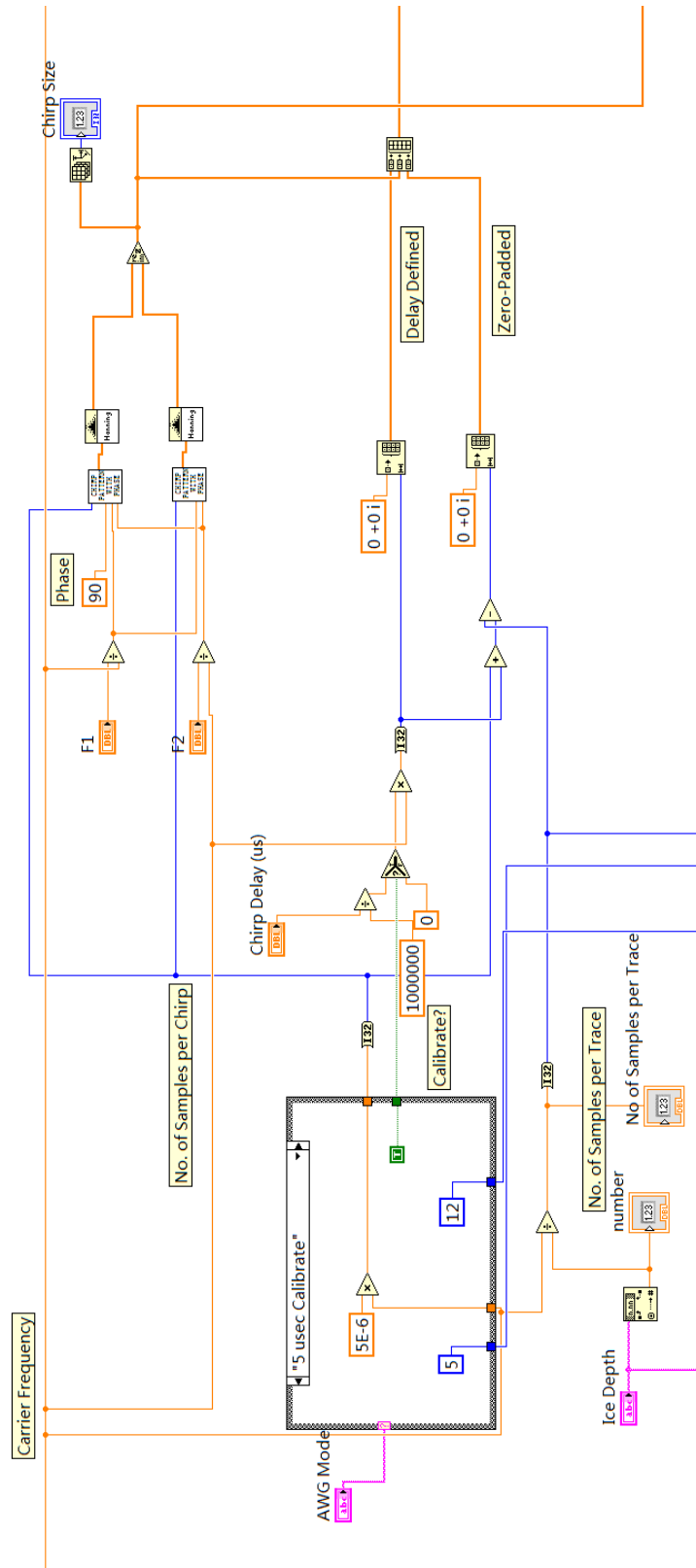


Figure 3-18 Block Diagram of Waveform Generation

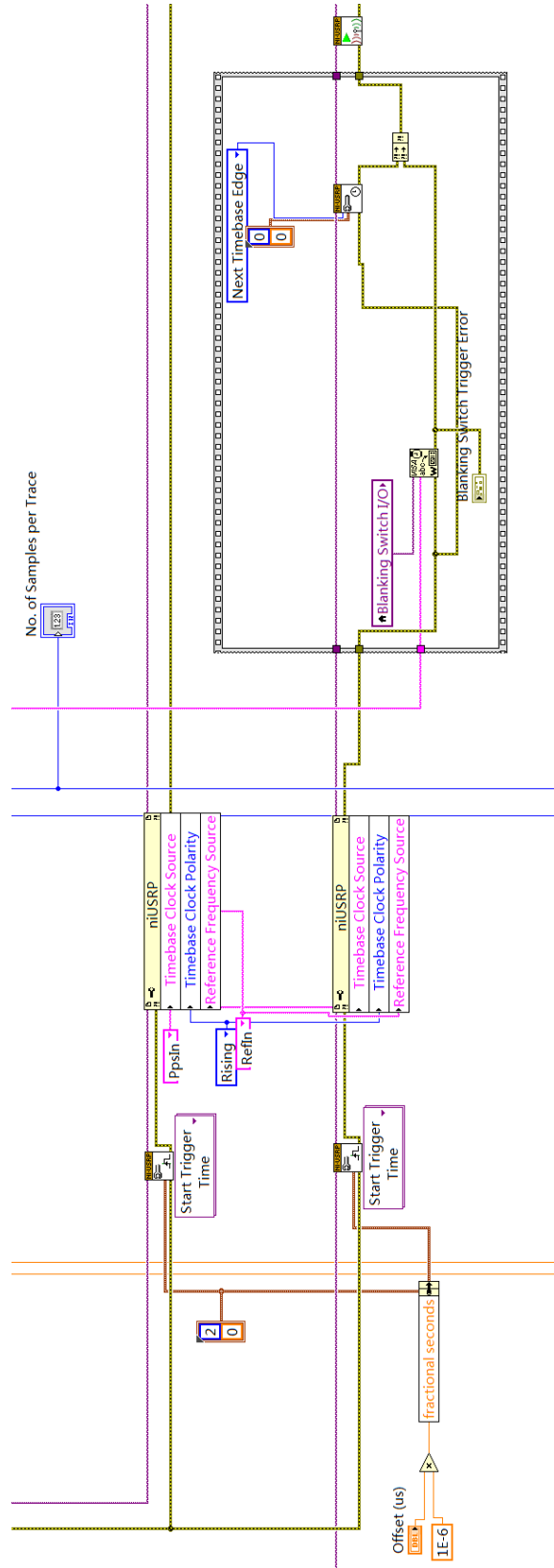


Figure 3-19 Block Diagram of TX/RX and External FPGA Synchronization

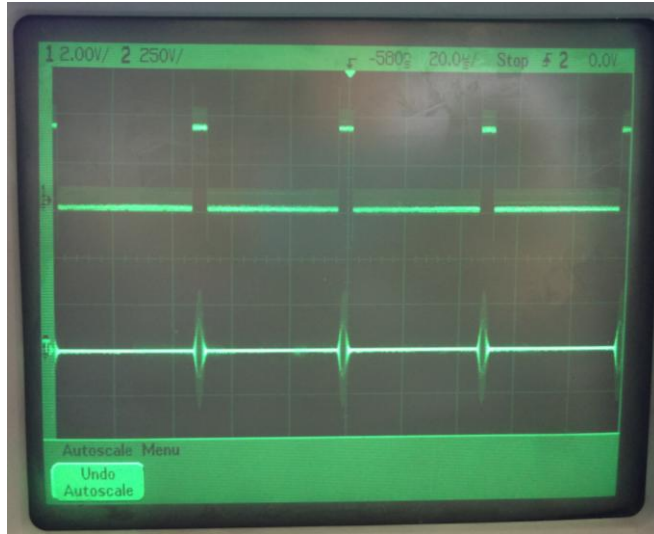


Figure 3-20 Chirp and Blanking Switch Control Synchronization

3.7.4 Data Acquisition Loop

The data acquisition loop uses the niUSRP Fetch RX Data VI to capture single channel complex data. The trace length is defined as the single trace length before concatenation, as stated in Section 3.7. The captured traces are added and averaged according to the number of coherent averages specified. For each averaged trace, trace display and matched filtering are carried out. The averaged trace is displayed through the Waveform Graph, with separate traces for real and imaginary parts. At the same time, the trace is correlated with the original I/Q chirp. One 32-bit-long integer is applied to work as a counter to the maximum value equal to the number of coherent averages. If the “Start Recording” button is pushed, then GPS information, the original trace, and the matched filtered trace are saved. Two unsigned 32-bit integers are initialized to zero, with one representing the number of files that have been written to hard disk, and the other representing the number of traces that have already been stored to files.

The matched filter is programmed using cross-correlation and peak detection VIs, combined with truncation according to the characteristic of the cross correlation. The write to file VI inherits the one that was used in the PXI-based Ice Radar, with minor modifications.

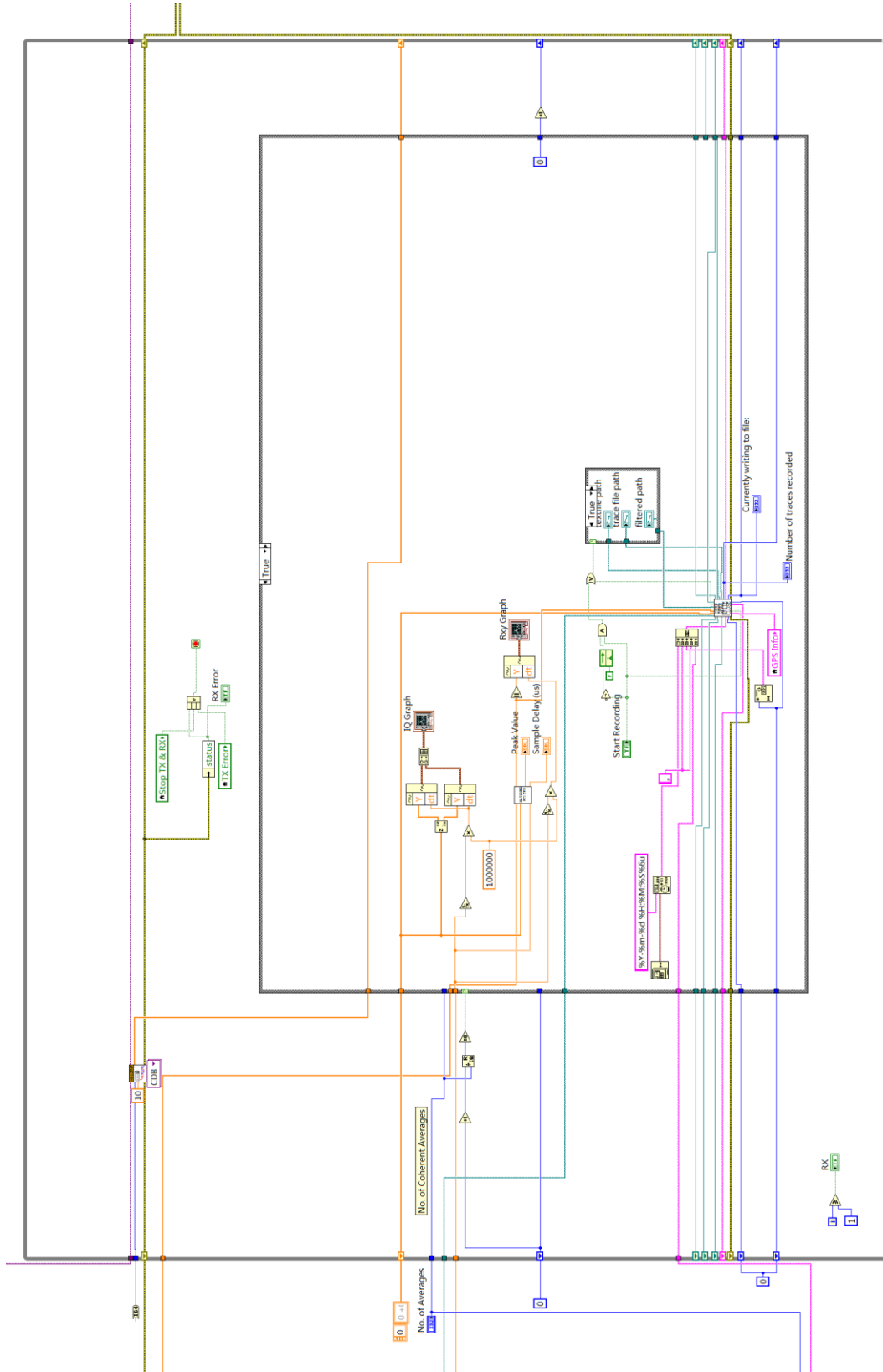


Figure 3-21 Block Diagram of Data Acquisition Loop

In this loop, there is no band pass filter added, which is different from the PXI-based Ice Radar, which applied a 24-bit Kaiser band pass filter. This decision is made based on a simple test result. When a band pass filter was added, the maximum allowable sampling rate was greatly decreased because of underflow error. So, to eliminate out-of-band noise, the traces could be extracted from files and run through a band pass VI with defined base band filter.

3.7.5 Matched Filter

The goal of the matched filter in this project is to achieve real-time processing of the captured traces, so as to target the reflected chirp location. With reference to Figure 3-22, the matched filter subVI is programmed by applying the 1D complex cross-correlation method, based on an FFT technique. The resulting trace is truncated due to the extended length caused by the cross correlation. If the chirp length is n , the first $(n - 1)$ values after the cross-correlation method are deleted. To obtain the peaks, the data first go through the Absolute Value Function to get the absolute values of all the trace data. Then, the Peak Detector VI is used to find the peaks and their locations within the waveform. As the peak detector function applies interpolations between data points, the actual outputs of the locations are not the actual integers representing the array index. To fit the indexes to the resolution, they are rounded to the nearest integers. In the meantime, the peak value array goes through the Array Max & Min function, which obtains the maximum value of the peaks and represents the peak value of the matched filtered trace and its location. Using this location value from the Array Max & Min function as the index of the location array from the Peak Detector, the peak location is obtained. Finally, combined with the Sampling rate, the sample delay is found.

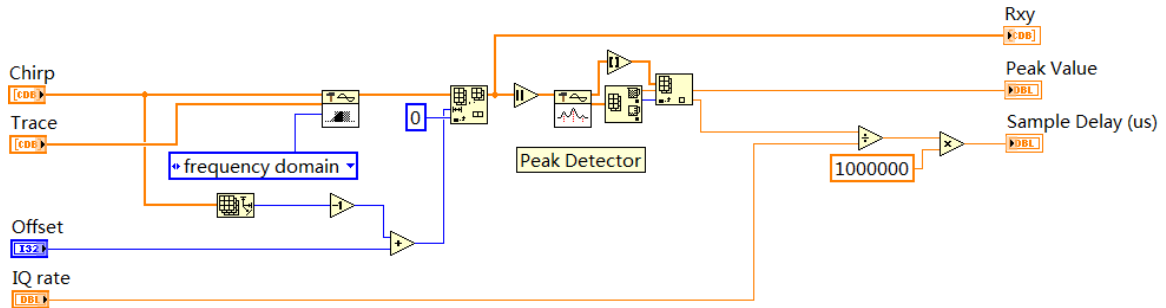


Figure 3-22 Block Diagram of Matched Filter Files

A button named “Start Recording” is placed on the Signal Configuration tab of the LabVIEW front panel. Before running the system, it can be selected as on or off. When the “Start Recording” button is on, three files for each storage will be created, with the format of file names initialized as “radar_%Y_%m_%d_%H_%M_%S_chan_%5d_”, followed by “0.txt”, ”1.dat”, or “2.dat”. In the file name, %Y, %m, %d, %H, %M, and %S represent the time information when the files start to be saved, corresponding to year, month, day, hour, minute, and second, while the %5d represent five digits starting from 00000, incrementing by 1 each time, representing the number of files that have been written to disk. The file “0.txt” contains information on the GPS, Computer Time, Trace Number, Sample Rate, Carrier Frequency, Number of Samples per Trace, Number of Averages, TX and RX Gains, Chirp Length in μs , and Chirp Frequency Range. As these information pieces are stored in string form in text files, they can be easily viewed simply by opening the files. The “1.dat” and “2.dat” files are used to save raw trace and matched-filtered trace data, correspondently. Both traces have complex double-precision samples, which means for each sample, both real and imaginary parts are 64-bit double-precision floating-point values. Thus, these two files contain binary data with each sample containing 128 bits.

For each set of three files, the averaged traces for 1000 traces are saved. Trace recovery can be carried out by calculation of single trace length based on information from “0.txt” file, combined with data type information as explained above. A data recovery program named “Read_IceRadar_Files_Read_trace_USRP.vi” is created to recover trace file from “2.dat”. By

typing in corresponding chirp parameters, recovered trace can also be obtained directly from this file.

Chapter 4 System Test

Based on the theoretical analyses and system design description, the RF Front-end circuit has been built. To make sure that the system works as designed, and to ensure all parts perform as expected, a series of tests have been implemented. These tests have been carried out in the Systems Design Laboratory and the Antenna Anechoic Chamber and Microwave Lab. An Agilent 54622D Mixed Signal Oscilloscope, Agilent E4408B Spectrum Analyzer, and Agilent E5071C Network Analyzer have been used to measure signals in both time and frequency domains, chirp & TTL synchronization, TX & RX front-end gains, and calibrate mode gain. The spectrum analyzer is also used to measure the output power from the USRP TX, and for chirp frequency selection in combination with the band pass filters.

The initial design applies three tubular BPFs from K & L Microwave, with part number 5B120-150/T10-O/O, which has center frequency of 150 MHz and 3 dB BW 10 MHz. The reason we need BPFs with 10 MHz BW instead of 5 MHz BW is that it is adaptive for future modification when a USRP with higher sampling rate is applied. According to Nyquist sampling theorem, the chirp bandwidth can be extended if sampling rate improves. Actual tests were carried out using two BPFs, a Trilithic 5BC160/20-3-KK with center frequency 160 MHz, and 3-dB BW of 10 MHz, and a K & L 3BT-95/190-5-N/N tunable BPF. By setting center frequency of the tunable BPF to 152.5 MHz, the pass band frequency range is 150–155 MHz. These replacement BPFs were used during testing due to a delay in obtaining the desired ones.

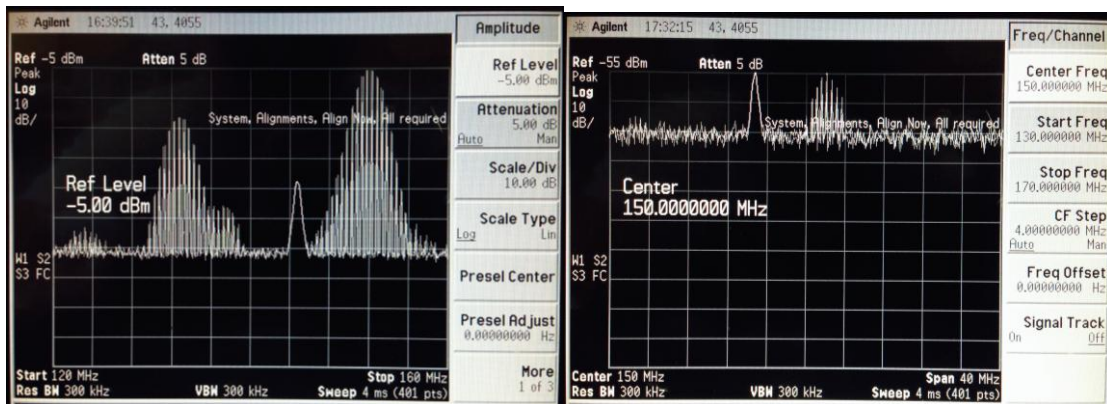
4.1 USRP Output Power Test

The USRP TX port output power is tested to ensure proper power level is input to the TX front end path, so that no damage occurs to the system. In the glacier mode, 0 dBm is output, while in the calibrate mode, -50 dBm is output.

As the daughterboard of the USRP is not calibrated, there is not a linear relationship between signal configuration and output power. So, the accurate signal power level has to be determined by testing and changing chirp amplitudes and TX gains. The signal power can be measured using

the spectrum analyzer. Because an adjustable attenuator is found on the signal going into the spectrum analyzer, which is used to protect the device from being damaged, the actual power input is the value displayed on the screen plus the attenuation value. To make the calibration efficient, for the glacier mode, a -5 dBm reference power level is set, which means the upper-most horizontal line on the screen represents -5 dBm signal power. As the attenuation is automatically set to be 5 dB, the 0 dBm signal power can be easily achieved just by changing TX gain (chirp amplitude is set to be 1). Once the chirp peak reaches the upper-most line, the output from USRP is 0 dBm. At this time, the TX gain value is the gain needed in the glacier mode.

For calibrate mode, the method is a bit different. The reference power level is set to be -55 dBm; so, with 5-dB attenuation, the actual input power is -50 dBm. When reducing TX gain to 0 dB, the chirp peak power is still -28 dBm. So, the chirp amplitude has to be decreased until peak power reaches the reference power limit. Test results are shown in Figure 4-1:



(a)

(b)

Figure 4-1 Spectrum Analyzer Display of USRP Outputs in (a) Glacier Mode (b) Calibrate Mode

The other tests are targeted on all the chirp lengths in both modes. The final results are listed in Table 4-1.

Table 4-1 Chirp Amplitudes and TX Gains in Different Modes

AWG Mode	Chirp Amplitude	TX Gain
1 μ s Calibrate	0.025	0
3 μ s Calibrate	0.013	0
5 μ s Calibrate	0.01	0
1 μ s Glacier	1	21
3 μ s Glacier	1	15
5 μ s Glacier	1	12

4.2 USRP Direct Power Arrival

To observe the performance of signal transmission and TX/RX synchronization accuracy, the TX and RX of the USRP are connected with two omni-directional antennas. It is stressed in the USRP specification sheet that the RX input power should not exceed 0 dBm. As the test result in Section 4.1 shows, when chirp amplitude is 1 and TX gain is 0, the chirp peak power is -28 dBm, thus no extra attenuator is needed at TX or RX if TX gain is set to 0. The direct power arrival test result without synchronization offset is shown in Figure 4-2. The Sample Delay shows the TX and RX has 1.85μ s, which means the RX starts 1.85μ s earlier than the TX.

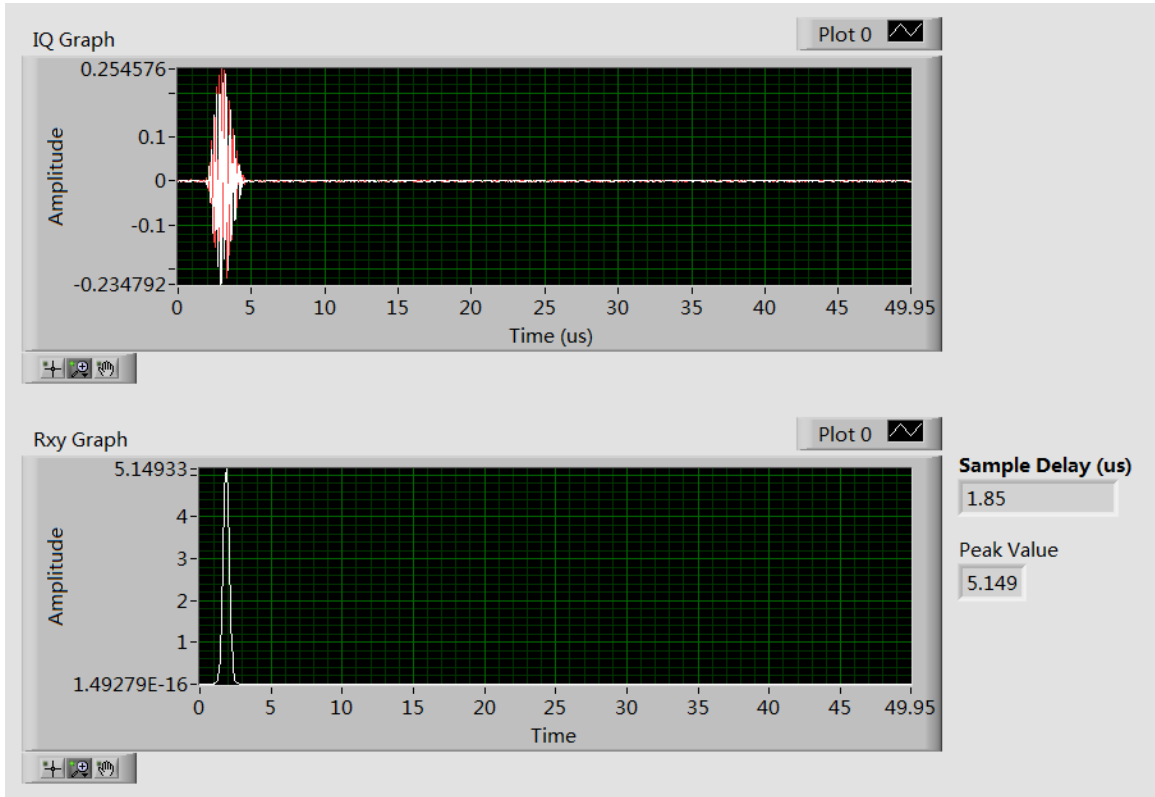


Figure 4-2 USRP Direct Power Arrival Test without Offset

This delay can be added to the RX synchronization timestamp, which means the RX timestamp is 2.00000185 s. This ensures TX and RX start simultaneously, as shown in Figure 4-3. It is clear that the peak value appears at 0 s in the Rxy Graph.

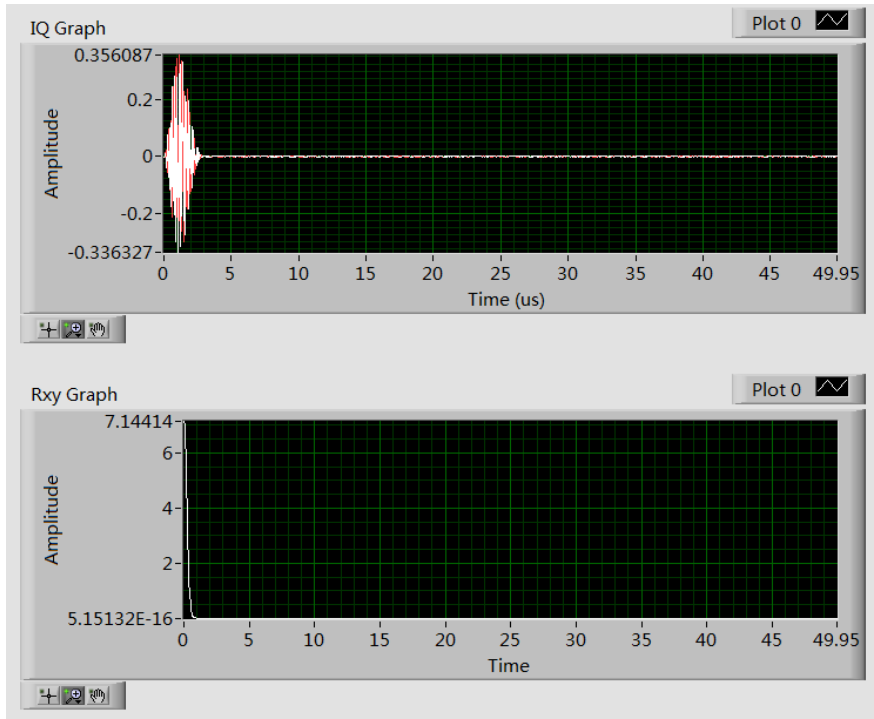


Figure 4-3 USRP Direct Power Arrival Test with Offset

To test the performance of USRP signal transmission with delay, a 10- μ s delay is added to the trace. The amplitude and TX gain are set as 1 and 0, which are the same as for the tests above. When offset value is applied, the result is in Figure 4-4. The peak in Rxy Graph shows up exactly at 10 μ s. This indicates that the programs and USRP are working correctly.

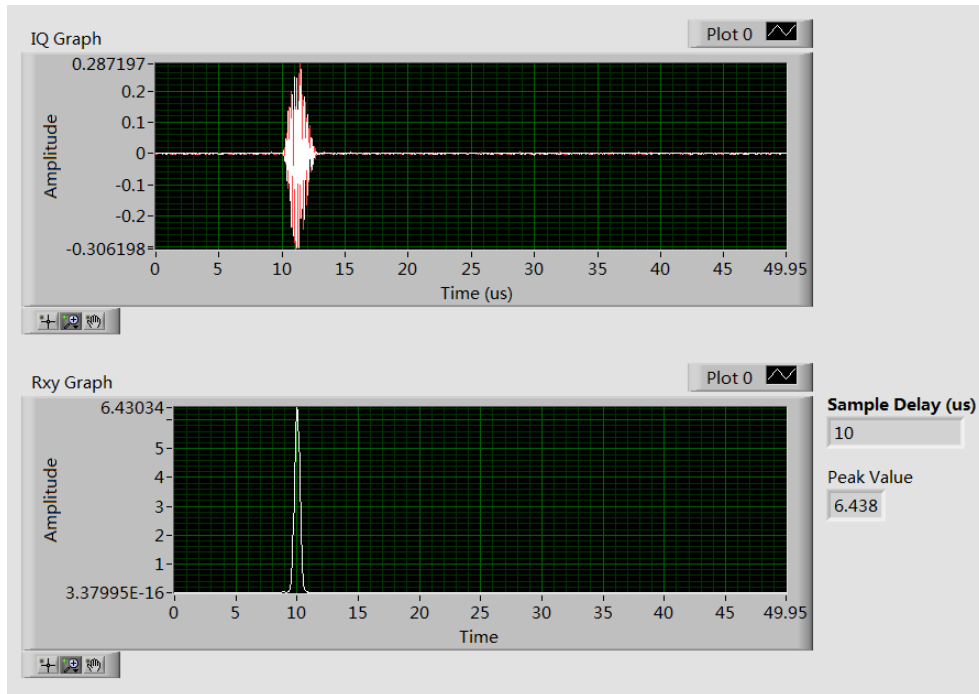


Figure 4-4 USRP Direct Power Arrival Test with Delay

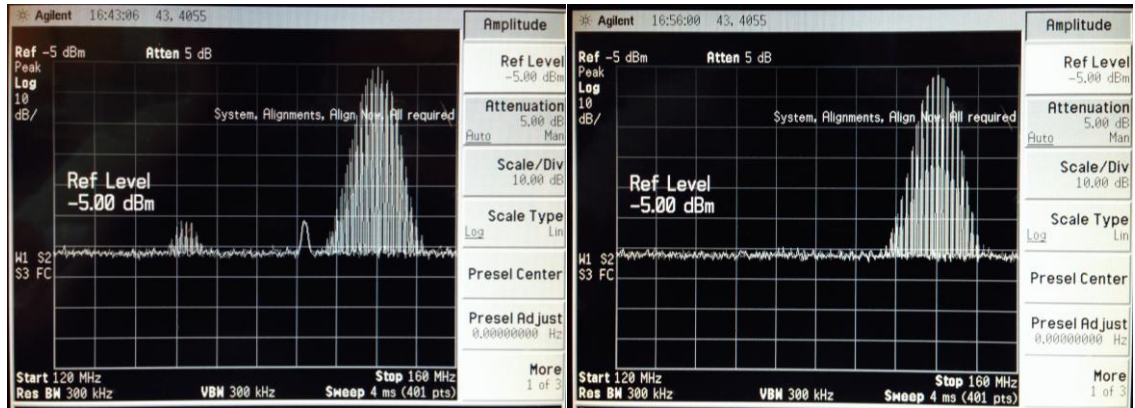
4.3 TX & RX Front-End Paths Tests

The TX and RX front-end paths are tested separately on an Agilent E5071C Network Analyzer, with main goal of observing the performance of the paths on pass/stop bands. The performance of band pass filters in filtering out the carrier frequency and aliasing components is also examined using the spectrum analyzer.

As the two band pass filters that were used for tests have different bandwidths and center frequencies, the tunable BPF is tuned with the left cut off frequency the same as the 20-MHz BW BPF (150 MHz), by setting the center frequency as 152.5 MHz. Also, since the carrier frequency and aliasing frequency components are mainly lower than 150 MHz, the observation during test is focused on the left part of the cut-off frequency of 150 MHz.

4.3.1 TX Front-End BPFs Performance Test

As shown in Figure 3-5 and Figure 4-1, carrier and aliasing components are output from USRP. To eliminate these components, tests on passing through single and double BPFs are both carried out, with the results presented in Figure 4-5 and Figure 4-6.



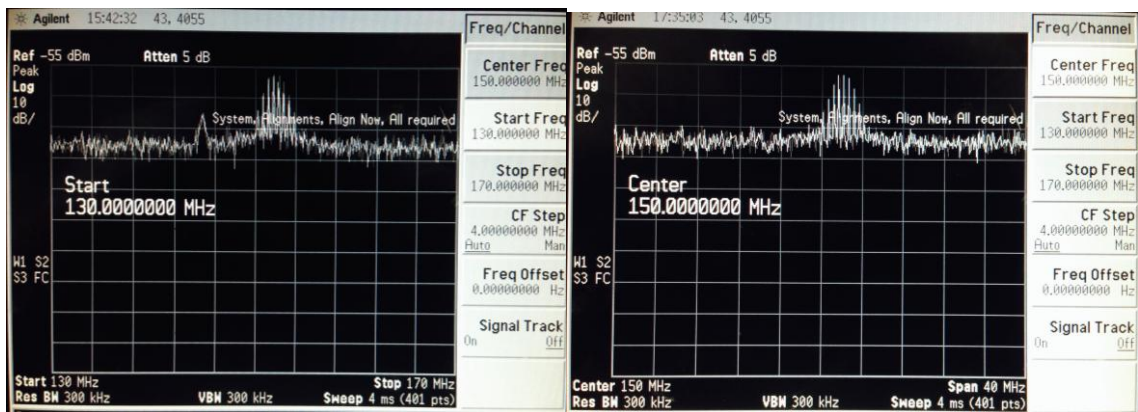
(a)

(b)

Figure 4-5 TX Front-End Band Pass Performance with Glacier Mode Output using (a) Single BPF (b) Double BPFs

Band pass performance can be easily observed by comparing Figure 4-1(a) and Figure 4-5. Carrier and aliasing components are greatly weakened with one BPF, but are still with detectable power. After going through the Power Amplifier, they will be strong and will cause damage to RX components. Only with 2 BPFs can those components be eliminated.

Situations are the same with calibrate mode output, as is shown in Figure 4-6.



(a)

(b)

Figure 4-6 TX Front-End Band Pass Performance with Calibrate Mode Output using (a) Single BPF (b) Double BPFs

4.3.2 TX Network Analysis

A test was carried out using the network analyzer on the TX front-end path. Port 1 of the network analyzer was connected to the input of the BPF, labeled as Node 1 in Figure 3-6, while

Port 2 was connected to the output of the second BPF, labeled as Node 18 in Figure 15. A power level of 0 dBm is set on network analyzer, and band pass performance is shown in Figure 4-7.

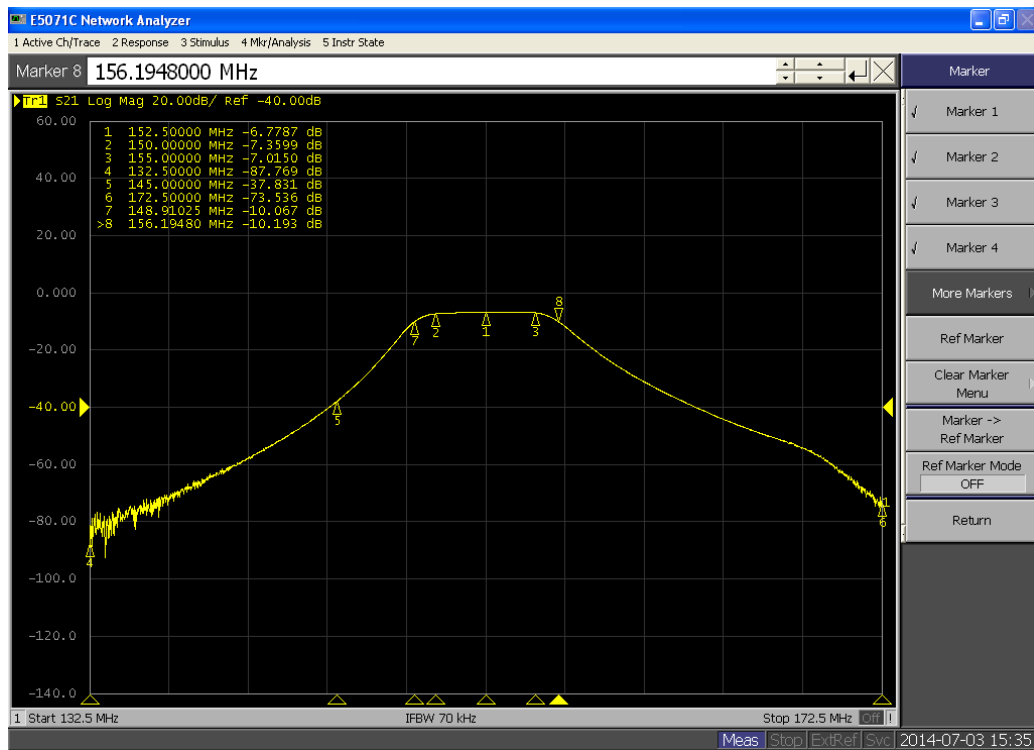


Figure 4-7 TX Front-End Path Band Pass Performance

The network analyzer frequency sweep range was set to 132.5–172.5 MHz, a pass band flatness of 0.5 dB is observed between 150 MHz and 155 MHz, with 6.8 dB attenuation at 152.5 MHz, 7.3 dB at 150 MHz, and 7.0 dB at 155 MHz. The attenuation at 145 MHz is 38 dB, which means the carrier frequency will see 38-dB attenuation. Attenuation keeps increasing, exceeding 58 dB when frequency is lower than 140 MHz, which is where aliased frequency components exist. Considering the power of the carrier frequency component is around -37 dBm, whereas that of the aliasing components is about -16 dBm, the attenuations are high enough to eliminate those components.

As TX path attenuation ranges from 6.8 to 7.3 dB between 150 MHz and 155 MHz, a -7 -dBm chirp signal can be obtained at the input of Power Amplifier, if setting USRP output as 0 dBm.

4.3.3 RX Network Analysis

The RX path test is implemented using the network analyzer, by connecting Port 1 to RX Input port, labeled as Node 19 in Figure 3-7, and Port 2 to output of limiter, labeled as Node 11 in Figure 3-7. As the minimum power level of the network analyzer is -55 dBm, to avoid saturation from the three amplifiers, attenuators are added before the RX path and between the amplifiers. When the network power level is set as -55 dBm, a 30-dB attenuator is connected between Port 1 of network analyzer and the first BPF at the RX path, as on Node 19 in Figure 3-7. Also, a 20-dB attenuator is placed between the first amplifier and the blanking switch, as on Node 6 in Figure 3-7, and two 5-dB attenuators between the second and third amplifiers, on Node 17. Therefore, the total attenuation added is 60 dB.

The band pass performance of the RX path is shown in Figure 4-8. From the plot, a flat gain is observed between 150 and 155 MHz, ranging from 31 to 32.3 dB. The 1.3-dB variation is acceptable. Also, at frequency ranges lower than 143 MHz and higher than 163 MHz, gain goes below 0 dB, giving the RX path good performance in filtering out noise power. Gain goes lower than -40 dB when frequency is lower than 133 MHz.



Figure 4-8 RX Front-End Path Band Pass Performance

Noticing that 60-dB attenuation is added during the test, a $60 + 32.3$ dB = 92.3 dB gain is expected from the receiver path. This value is close to the gain shown in Figure 3-12, where the gain between Node 19 and 13 is calculated as 91.5 dB. Compared to the test result of the PXI-based Ice Radar, the USRP-based radar improves the RX path gain by 19 dB.

4.4 Blanking Switch and Glacier/Calibrate Mode Selection

The blanking switch module is controlled by the external FPGA. To avoid excessive noise introduced by the amplifiers, the blanking switch module was tested by disconnecting all amplifiers, leaving the remainder of the components in the RF front-end paths. Also, two omni-directional antennas are installed at TX Out and RX In ports.

In this test, the blanking switch and glacier/calibrate mode selection were tested at the same time. When system and chirp modes are selected, external FPGA outputs TTL-High/TTL-Low for mode selection, and periodic TTL-High/TTL-Low blanking switch control signals are output to the four switches.

In both glacier and calibrate modes, the blanking switch module is turned on in the beginning, with duration defined by the chirp length. So in the glacier mode, when blanking switch works, no chirp signal can be seen on IQ Graph. In the calibrate mode, chirp delay can be changed from 0 to 30 μs . Thus, as long as chirp starts to be transmitted 3 μs after TX starts, a chirp will be seen.

Figure 4-9 shows the state when the blanking switch is working in the glacier mode. To make sure the leakage from blanking switch is seen, no offset is added to the RX start time. So, the leakage pulses from around 2 μs and 5 μs can be identified from the plot. This shows a good blanking effect on the captured chirp.

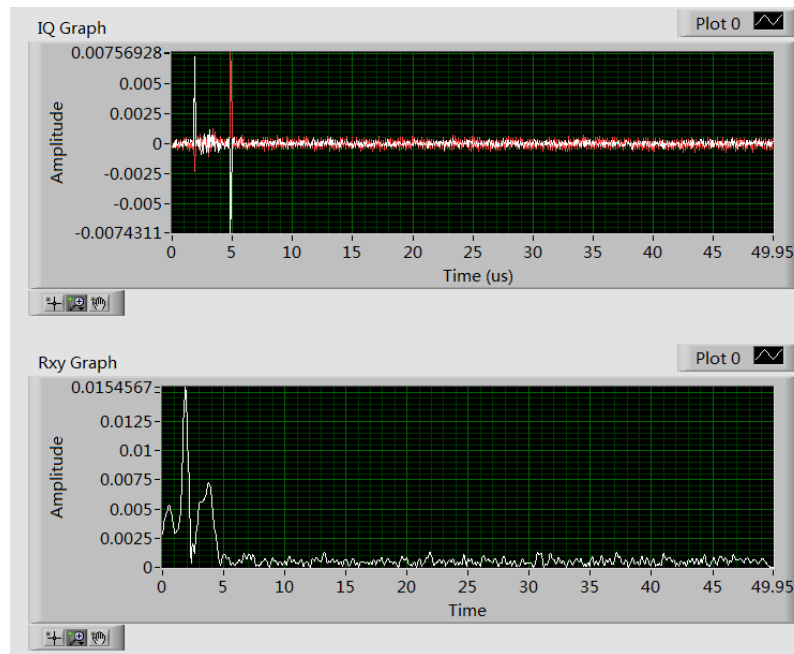


Figure 4-9 Blanking Switch State in Glacier Mode

To check the calibrate mode, three tests were implemented, which added 10 μs , 1.5 μs , and 0 μs delays to the chirps. To make sure Sample Delay shows correct time delay, 1.9 μs offset was added to the RX start time. The calibrate mode tests were carried out using a 3- μs chirp with 50- μs trace length. As the amplifiers were removed from the RX path, to ensure a large enough signal was received, the chirp amplitude was changed from 0.013 to 1, and TX gain was increased to 15. At the same time, attenuation between TX and RX switch on calibrate path was

reduced from 40 to 20 dB. These changes allowed the test results shown from Figure 4-10 to Figure 4-12.

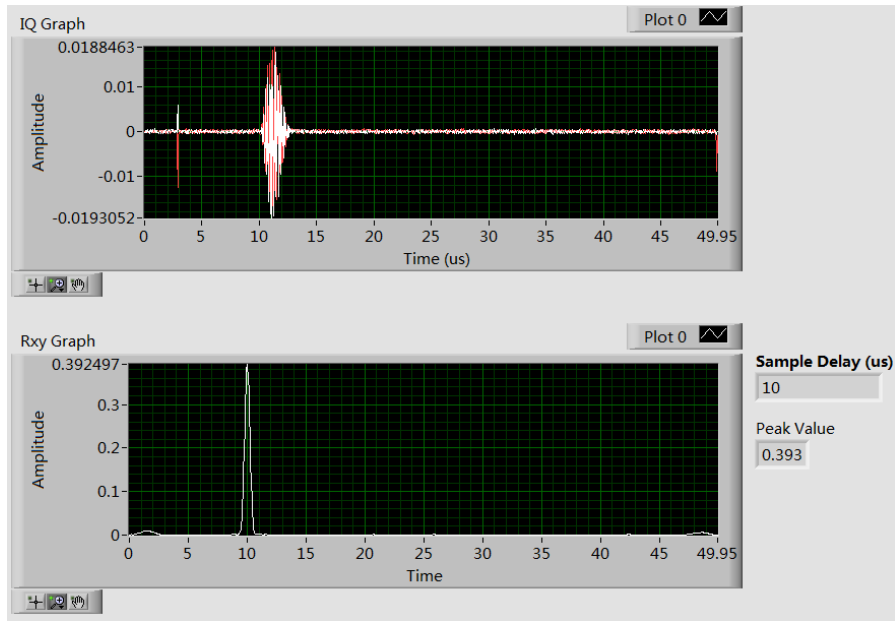


Figure 4-10 Blanking Switch State in Calibrate with 10 μ s Delay

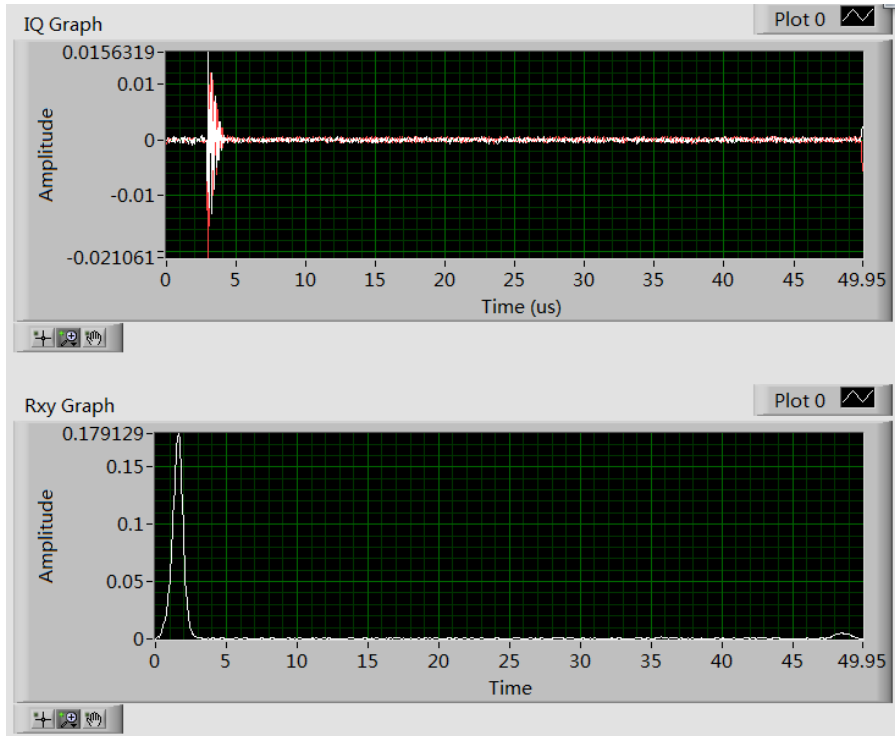


Figure 4-11 Blanking Switch State in Calibrate with 1.5 μ s Delay

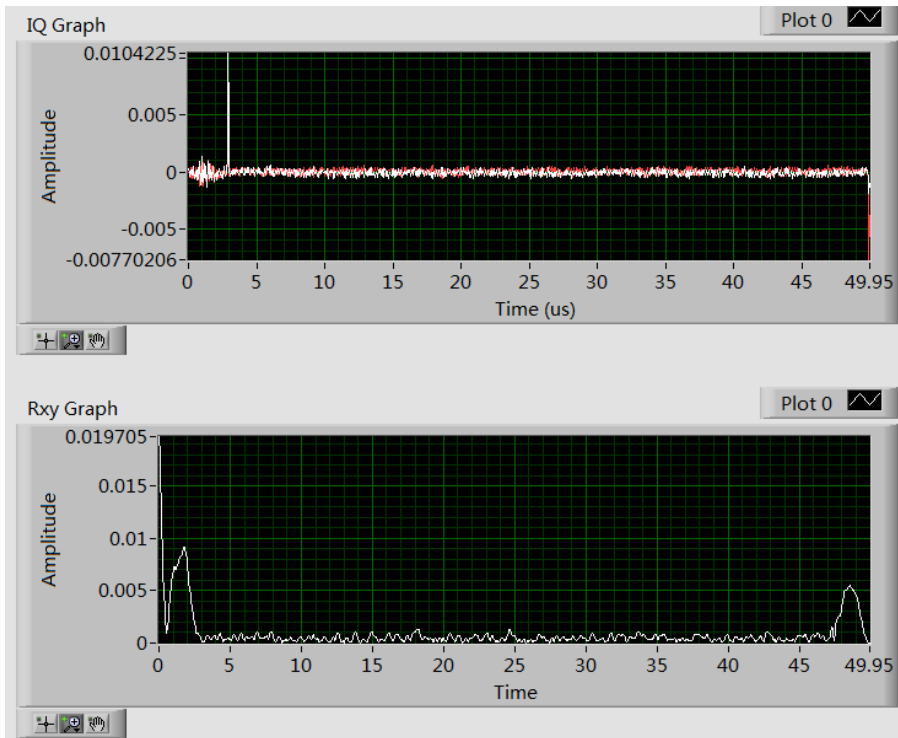


Figure 4-12 Blanking Switch State in Calibrate without Delay

Leakage from the blanking switch can still be identified at 3 μs in all the three figures above, which indicates the blanking switch worked for all the three situations. From Figure 4-10, a clear chirp can be seen from 10 μs to 13 μs . In Figure 4-12, no significant chirp is seen, which means blanking switch works on the first three microseconds in the calibrate mode. Including the result in Figure 4-9, the conclusion can be made that blanking switch works in both calibrate and glacier modes. The 1.5- μs delay was added to the trace, mainly to make a comparison between the waveform before 3 μs and the half chirp after 3 μs , as is shown in Figure 4-11. It is apparent that chirp before 3 μs was blocked, while signal after then was well kept, so no side effect was brought to the received signals by the blanking switch module.

The tests in this section demonstrate that both the blanking switch and mode selection modules work well. Equipped with these two modules, system will be well protected from being damaged by excessive power.

4.5 Delay Line Test

To test whether this USRP-based Ice Radar can accurately detect the delay in signal transmission, a delay line test was implemented. An RFC400 coaxial cable was used as the signal transmission channel, and two additional SMA cables were later connected to the RFC400 during a second test to add additional length. The TX Out and RX In ports were directly connected to the two ports of the delay line, and the blanking switch was manually disabled by disconnecting the control signal cable. An offset of 2 μs was added due to the extra delay introduced by the RX front-end paths.

The accuracy of the system detection is evaluated by comparing the measurement time difference between measurement results from the USRP-based radar, the PXI-based radar, and the network analyzer. If result differences are within the sampling period of the USRP, the accuracy of the USRP-based radar is acceptable. Test results of PXI-based radar and the network analyzer are from [14]. So, comparisons can be made from Table 4-2:

Table 4-2 Delay Line Test Results

System	Time Delay (μs)	Estimated Cable Length (ft) ($v = 0.85c$)
Network Analyzer	1.0628	889.15
PXI-based Ice Radar	1.0640	890.16
USRP-based Ice Radar	1.05	878
Network Analyzer (2 SMA ext.)	1.0779	901.80
PXI-based Ice Radar (2 SMA ext.)	1.0800	903.54
USRP-based Ice Radar (2 SMA ext.)	1.10	920

As the sampling rate of the USRP is 20 MHz, the sampling period is 0.05 μs . The time delay difference between USRP-based radar and network analyzer, and between USRP-based radar and PXI-based radar, are 0.0128 μs and 0.0140 μs , which are smaller than 0.025 μs . After extension, the time delays measured by the network analyzer and PXI-based radar were closer to 1.10 μs than to 1.05 μs , considering the resolution of the USRP-based radar. From the USRP-based radar

side, the test result is also 1.10 μs . So, a conclusion can be made that the detection accuracy is within the closet value.

Chapter 5 Discussion

This project has designed and integrated an Ice Radar that transmits chirp signals with frequency range from 147.5 to 152.5 MHz, selectable pulse repetition frequency (PRF) of 100 kHz, 40 kHz, and 20 kHz, and a coherently-averaged result from 65,536 returns. Parameters of the system can be adjusted according to changes in the BPFs, laptop performance, and even upgrades of the USRP.

During system tests, several issues have been identified in the system design. Some have a positive impact on the system while others do not. These issues are discussed below, along with advances of this radar design when compared to the PXI-based radar.

In-lab tests have been carried out by adjusting the chirp frequency range to 150–155 MHz, due to the delay in receiving the correct band pass filters. As only two suitable band pass filters are available, while TX and RX paths need two BPFs each, the TX and RX tests have to be performed separately, each time with BPFs disconnected from one path and integrated into the other. Test results show that both TX and RX paths work with flat gain at pass band, and stop band performance is very good.

Tests that involved both TX and RX paths with only two BPFs showed a high noise level, which comes from RX amplifiers. When the blanking switch tests were performed, the amplifiers were disconnected, and good results were obtained. The noise issue is solved by adding BPFs to the RX path.

Another issue with the BPFs is that, when connecting only one BPF to the TX path, the carrier and aliasing frequency components could not be eliminated. If the carrier frequency goes through the power amplifier, a strong signal will be generated that will cause damage to the RX path, especially to the amplifiers. This is why two BPFs are needed for the TX path.

Measuring the TX path gain in the operating frequency range shows that the gain at 152.5 MHz is -6.8 dB, which is close to the design goal of -7 dB. This test result was obtained

by replacing the 2-dB attenuator to a 3-dB one. This shows that the TX path components have lower insertion losses than the values stated on the datasheet.

There is a tricky issue with the TX and RX LED indicators on the LabVIEW front panel, as is shown in Figure 5-1. Normally, TX lights up earlier than RX. Experience indicates that, if the software is immediately run after changes are made to parameters—especially for those USRP configuration parameters, such as TX gain, RX gain, I/Q rate, and offset—RX will light up earlier, while no Error LED is lit up. In this situation, RX will just receive noise signals. It will usually take three runs and stops of the software until system starts to work normally. More work will need to be done to determine why this is happening, but it is likely due to timing.

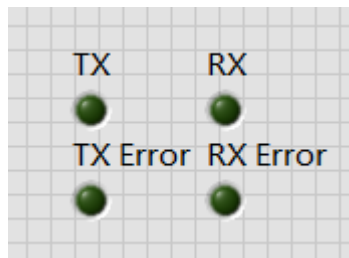


Figure 5-1 TX & RX LEDs

Power supplies to the RF front-end components require voltages of GND, -5 V, 5 V, and 15 V. These voltages are the same as those used in the PXI-based Ice Radar. Considering a standardized Power Box was later built up for the PXI-based radar front-end box, with 9-pin serial port, it can be directly applied in the USRP-based Ice Radar.

Compared to the PXI-based radar, the USRP-based radar has the advantage of fewer TX front-end components needed, and it has 19-dB higher gain in RX front-end path. But due to the removal of the step attenuator, no adjustments in gain can be made in the RX front-end, which is not good for shallow ice detection. This drawback has to be overcome by reducing the TX gain of USRP, which leads to the reduction of TX power from TX antenna.

Chapter 6 Conclusion and Future Work

The USRP-based Ice-penetrating Software-defined Radar (“USRP-based Ice Radar”) has been designed and built and several initial tests on the system have been performed. Background material, theoretical analysis, and system design and test are documented in this thesis. Signal configuration and properties of the USRP hardware can be directly defined through LabVIEW, giving the system flexibility for future implementations. Also, by changing the signal frequency range via LabVIEW and replacing the band pass filters in the RF front-end box, a change in the signal frequency range can be implemented. This project inherits development techniques from the PXI-based Ice Radar, but achieves greater portability and flexibility. Field measurements in the Antarctic will be carried out, providing data for ice sheet depth changes and glacier movement.

Although in-lab tests have demonstrated the proper functioning of the system, future work on the system is still required. Specifically:

1. High performance laptop is needed.

As was discussed in Section 3.1, a higher performance laptop (or single board computer) is needed to obtain the maximum bandwidth possible from the USRP.

2. Band pass filters are needed for TX and RX paths.

Before final integration of the Ice Radar system, four BPFs are needed to replace the ones that were used for in-lab tests. The desired BPFs are from K & L Microwave, with part number 5B120-150/T10-O/O, which has center frequency of 150 MHz and 3-dB BW of 10 MHz. These BPFs also allow for future system upgrades using the NI USRP RIO.

3. Power supply for USRP and external FPGA needs to be designed.

As the Power Box of the PXI-based Ice Radar does not provide a 6-V power supply, the Power Box of the USRP-based Ice Radar should include 12-V-to-6-V DC–DC

converter. Current requirements of the 6-V power supply need to be determined according to USRP and external FPGA specifications.

4. RF Front-end size can be further reduced if Surface-Mount Technology is applied.

Surface-Mount Technology should be used to integrate the components of the RF front-end circuit onto a small board, which will save much more weight and space, resulting in more portability.

5. NI USRP RIO can be used rather than the USRP 2920. A method for PCIe connection between host and USRP must be determined.

The NI USRP RIO allows as high as 800 MB/s communication with the host, if equipped with PCI Express $\times 4$ connection. Commonly, this is not found in a laptop. So research needs to be done on connections between the USRP and the laptop, or other host. The USRP RIO also provides direct access to its FPGA from within LabVIEW, which will eliminate the need for the external FPGA.

When changing out the USRP 2920 with the NI USRP RIO, almost all the code written for this project can be directly applied. The use of the NI USRP RIO will also greatly increase the sampling rate and chirp bandwidth.

Appendix: Bill of Materials

Table A-1 Bill of Materials

Component	Qty.	Description	Supplier	Part No.
BPF	4	CF 150 MHz, 3-dB BW 10 MHz, IL 2.4 dBa, Stopband Atten: 130 MHz 48 dBc, 170 MHz 53 dBc	K & L	5B120-150/T10-O/O
Switch	2	TTL control, SPDT, IL 1.1 dB, 1-dB compression 18 dBm, Power: ± 5 V	Mini Circuits	ZYSWA-2-50DR
Switch	2	TTL control, SPDT, IL 1.3 dB, 1-dB compression 17 dBm, Power: ± 5 V	Mini Circuits	ZASWA-2-50DR
PA	1	Gain 50 dB with P1dB 48 dBm *Includes heat sink dim 10 \times 7.3 \times 6.3 in ³ Case Style: BT1165	Mini Circuits	ZHL-50W-52S
Amplifier	2	1-600 MHz, Gain:52 dB (45 dB tested), NF:1.5 dB, P1dB Out: 12 dBm	Miteq	AU-1027
Amplifier	1	10-500 MHz, Gain: 14 dB (12.5 dB tested), NF: 3.4 dB, P1dB Out: 9 dBm	Miteq	AU-1102
Power Combiner	1	10-2000 MHz, IL: 0.3 dB, Isolation: 30 dB	Mini Circuits	
Terminator	1	DC-2 GHz, Impedance: 50 Ω , Power Rating: 0.25 W	Mini Circuits	STRM-50
Limiter	1	DC-1.8 GHz, Max Input Pulse Power: 100 W, Max Input Average Power: 10 W, 1dB compression: 0 dBm.	HP	5086-7284
Attenuator	3	DC-6 GHz, 3 dB attenuation, Power Rating: 1 W	Mini Circuits	VAT-3+
Attenuator	2	DC-18 GHz, 20 dB attenuation, Power Rating: 5W	Mini Circuits	BW-S20W5+
Antenna	2	105 – 1300 MHz, Gain: 11 – 13 dBi	Create	CLP5130-2N

References

- [1] National Academy of Sciences, The Royal Society, “Climate Change Evidence & Causes: An overview from the Royal Society and the US National Academy of Sciences,” Internet: <http://dels.nas.edu/resources/static-assets/exec-office-other/climate-change-full.pdf>.
- [2] Stocker, T.F., D. Qin, G.K. Plattner, M. Tignor, S.K. Allen, J. Boschung, A. Nauels, Y. Xia, V. Bex, and P.M. Midgley, *IPCC, 2013: Climate Change 2013: The Physical Science Basis. Contribution of Working Group I to the Fifth Assessment Report of the Intergovernmental Panel on Climate Change*, Cambridge University Press, Cambridge, United Kingdom and New York, NY, USA, 2013.
- [3] V. V. Bogorodski, C. R. Bentley, and P. E. Gudmandsen, *Radioglaciology*, Hingham, MA: Kluwer Academic Publishers, 1985.
- [4] Knut Christianson, Robert W. Jacobel, Huw J. Horgan, Sridhar Anandakrishnan, and Richard B. Alley, “Subglacial Lake Whillans—Ice-penetrating radar and GPS observations of a shallow active reservoir beneath a West Antarctic ice stream,” *Earth and Planetary Science Letters*, pp. 237–245, 2012.
- [5] Joseph Mitola, “The software radio architecture,” *IEEE Communications Magazine*, vol. 33, no. 5, pp. 26–38, May 1995.
- [6] Asad A. Abidi, “The path to the software-defined radio receiver,” *IEEE Journal of Solid-State Circuits*, vol. 42, pp. 954–966, May 2007.
- [7] Ruihui Di, Senlin Peng, S. Taylor, and Y. Morton, “A USRP-based GNSS and interference signal generator and playback system,” *2012 IEEE/ION. IEEE Position Location and Navigation Symposium (PLANS)*, pp. 470–478, Apr. 2012.
- [8] M. Liso Nicolas, I. Artamonov, and T. Kurner, “Low-cost USRP SDR receiver for the investigation of multipath influence on GNSS systems,” *2013 7th European Conference on Antennas and Propagation (EuCAP)*, pp. 2300–2304, Apr. 2013.
- [9] A. Mate, Kuo-Hao Lee, and I-Tai Lu, “Spectrum sensing based on time covariance matrix

- using GNU radio and USRP for cognitive radio,” *2011 IEEE Long Island Systems, Applications and Technology Conference (LISAT)*, pp. 1–6, May 2011.
- [10] O. Ozdemir, R. Hamila, and N. Al-Dhahir. “A USRP-based experimental testbed for OFDM systems impaired by I/Q imbalance,” *2013 7th IEEE GCC Conference and Exhibition (GCC)*, pp. 98–102, Nov. 2013.
- [11] A. Blad, E. Axell, and E.G. Larsson, “Spectrum sensing of OFDM signals in the presence of CFO: New algorithms and empirical evaluation using USRP,” *2012 IEEE 13th International Workshop on Signal Processing Advances in Wireless Communications (SPAWC)*, pp. 159–163, Jun. 2012.
- [12] A. Prabaswara, A. Munir, and AB. Suksmono, “GNU Radio based software-defined FMCW radar for weather surveillance application,” *2011 6th International Conference on Telecommunication Systems, Services, and Applications (TSSA)*, pp. 227–230, Oct. 2011.
- [13] J. Ralston and C. Hargrave, “Software defined radar: An open source platform for prototype GPR development,” *2012 14th International Conference on Ground Penetrating Radar (GPR)*, pp. 172–177, 4–8 Jun. 2012.
- [14] Jesus Mendoza, “Development of an Ice-penetrating Software-defined Radar,” M.S. thesis, The Pennsylvania State University, USA, 2012.
- [15] Leon Osborne, Jeffrey Brummond, Robert Hart, Mohsen Zarean, and Steven Conger, *Clarus: Concept of Operations*, No. FHWA-JPO-05-072, Oct. 2005.
- [16] Matthew E. Peters, Donald D. Blankenship, and David L. Morse, “Analysis techniques for coherent airborne radar sounding: Application to West Antarctic ice streams,” *Journal of Geophysical Research: Solid Earth*, vol. 110, 2005.
- [17] David R. Dunson, “A wideband synthetic aperture radar for ice sheet basal measurements,” B.S. thesis, University of Kansas, USA, 1999.
- [18] Donald E. Barrick, William D. Stuart, and Clarence K. Krichbaum, *Radar Cross Section Handbook*. vol. 1. New York: Plenum Press, 1970.

- [19] John D. Paden, Christopher T. Allen, Sivaprasad Gogineni, Kenneth C. Jezek, Dorte Dahl-Jensen, and Lars B. Larsen, "Wideband measurements of ice sheet attenuation and basal scattering," *IEEE Geoscience and Remote Sensing Letters*, vol. 2, no. 2, pp. 164–168, Apr. 2005.
- [20] Christian Matzler, and Urs Wegmuller, "Dielectric properties of freshwater ice at microwave frequencies," *Journal of Physics D: Applied Physics*, vol. 20, no. 12, pp. 1623–1630, 1987.
- [21] Takeshi Matsuoka, Shuji Fujita, and Shinji Mae. "Effect of temperature on dielectric properties of ice in the range 5–39 GHz," *Journal of Applied Physics*, vol. 80, no. 10, pp. 5884–5890, Nov. 1996.
- [22] Shuji Fujita, Takeshi Matsuoka, Toshihiro Ishida, Kenichi Matsuoka, and Shinji Mae, "A summary of the complex dielectric permittivity of ice in the megahertz range and its applications for radar sounding of polar ice sheets," *Physics of Ice Core Records*, pp. 185–212, 2000.
- [23] Joseph A. MacGregor, Dale P. Winebrenner, Howard Conway, Kenichi Matsuoka, Paul A. Mayewski, and Gary D. Clow, "Modeling englacial radar attenuation at Siple Dome, West Antarctica, using ice chemistry and temperature data," *Journal of Geophysical Research: Earth Surface (2003–2012)*, vol. 112, 2007.
- [24] Constantine A Balanis, *Advanced Engineering Electromagnetics*, 4th edition, New York: Wiley, 1989.
- [25] David Jeffrey Griffiths, *Introduction to Electrodynamics*. 3rd edition, Upper Saddle River, NJ: Prentice Hall, 1999.
- [26] M. L. Zahn, *Electromagnetic Field Theory: A Problem Solving Approach*, New York: Wiley & Sons, 1985.
- [27] John Paden, "Synthetic aperture radar for imaging the basal conditions of the polar ice sheets," B.S. and M.S. thesis, University of Kansas, USA, 2006.

- [28] Joint Chiefs of Staff. *Department of Defense Dictionary of Military and Associated Terms*, Joint Chiefs of Staff Pub, 12 Apr. 2001.
- [29] National Instruments, “NI USRP 292X/293X Datasheet,” Internet: <http://sine.ni.com/ds/app/doc/p/id/ds-355/lang/en>, Apr. 14, 2014
- [30] Peter Vizmuller, *RF Design Guide: Systems, Circuits, and Equations*, Norwood, MA: Artech House, Jan. 1995.
- [31] S. Costanzo, F. Spadafora, A. Borgia, H. O. Moreno, A. Costanzo, and G. Di Massa, “High resolution software defined radar system for target detection,” *Journal of Electrical and Computer Engineering*, vol. 2013, 2013.
- [32] National Instruments, “I and Q Represented in Polar Form,” Internet: <http://www.ni.com/white-paper/4805/en/>, Feb. 06, 2014.
- [33] National Instruments, “Hardware Diagram of an I/Q Modulator,” Internet: <http://www.ni.com/white-paper/4805/en/>, Feb. 06, 2014.
- [34] William Arthur Blake, “Interferometric Synthetic Aperture Radar (INSAR) for Fine-Resolution Basal Ice Sheet Imaging,” Ph.D. Dissertation, University of Kansas, USA, 2010.